AFRL-AFOSR-UK-TR-2016-0033

Innovative Wing Structures for Improved Aerodynamic and Aeroelastic Perf 140081

Jonathan Cooper
THE UNIVERSITY OF BRISTOL

06/09/2016
Final Report

DISTRIBUTION A: Distribution approved for public release.

Air Force Research Laboratory
AF Office Of Scientific Research (AFOSR)/ IOE
Arlington, Virginia 22203
Air Force Materiel Command

REPORT DOCUMENTATION PAGE

Form Approved
OMB No. 0704-0188

The public reporting burden for this collection of information is estimated to average 1 hour per response, including the time for reviewing instructions, searching existing data sources, gathering and maintaining the data needed, and completing and reviewing the collection of information. Send comments regarding this burden estimate or any other aspect of this collection of information, including suggestions for reducing the burden, to Department of Defense, Executive Services, Directorate (0704-0188). Respondents should be aware that notwithstanding any other provision of law, no person shall be subject to any penalty for failing to comply with a collection of information if it does not display a currently valid OMB control number.

PLEASE DO NOT RETURN YOUR FORM TO THE ABOVE ORGANIZATION.

1. REPORT DATE *(DD-MM-YYYY)*	2. REPORT TYPE	3. DATES COVERED *(From - To)*
27-10-2016	Final	01 Jul 2014 to 30 Jun 2016

4. TITLE AND SUBTITLE
Innovative Wing Structures for Improved Aerodynamic and Aeroelastic Performance

5a. CONTRACT NUMBER

5b. GRANT NUMBER
FA9550-14-1-0081

5c. PROGRAM ELEMENT NUMBER
61102F

6. AUTHOR(S)
Jonathan Cooper

5d. PROJECT NUMBER

5e. TASK NUMBER

5f. WORK UNIT NUMBER

7. PERFORMING ORGANIZATION NAME(S) AND ADDRESS(ES)
THE UNIVERSITY OF BRISTOL
SENATE HOUSE, TYNDALL AVENUE
BRISTOL, BS8 1TH GB

8. PERFORMING ORGANIZATION REPORT NUMBER

9. SPONSORING/MONITORING AGENCY NAME(S) AND ADDRESS(ES)
EOARD
Unit 4515
APO AE 09421-4515

10. SPONSOR/MONITOR'S ACRONYM(S)
AFRL/AFOSR IOE

11. SPONSOR/MONITOR'S REPORT NUMBER(S)
AFRL-AFOSR-UK-TR-2016-0033

12. DISTRIBUTION/AVAILABILITY STATEMENT
A DISTRIBUTION UNLIMITED: PB Public Release

13. SUPPLEMENTARY NOTES

14. ABSTRACT
The use of novel wing internal structure to control and improve aeroelastic (static shape, flutter / divergence and gust response) wing performance was investigated. Rib and spar variable orientation and crenellation concepts were explored making use of NASTRAN Finite Element and MATLAB tools developed as part of the work. The report focuses on the spar/rib arrangement and the crenellated skin concepts. It was shown how it is possible to increase the flutter speed and also reduce gust loads via these non-conventional structural configurations. An experimental investigation examined the behavior of 3D printed wings in a series of wind-off and wind-on experiments, and whilst the general behavior validated the numerical predictions, there was a significant scatter on the results.

15. SUBJECT TERMS
EOARD, Topology Optimization, Wing Structure, Additive Manufacturing

16. SECURITY CLASSIFICATION OF:			17. LIMITATION OF ABSTRACT	18. NUMBER OF PAGES	19a. NAME OF RESPONSIBLE PERSON
a. REPORT	b. ABSTRACT	c. THIS PAGE			GARNER, DAVID
Unclassified	Unclassified	Unclassified	SAR	53	19b. TELEPHONE NUMBER *(Include area code)* 011-44-1895-616021

Standard Form 298 (Rev. 8/98)
Prescribed by ANSI Std. Z39.18

Innovative Wing Structures for Improved Aerodynamic and Aeroelastic Performance

Final Report

EOARD Contract: FA9550-14-1-0081

J. E. Cooper[1], G. Francois[2]

Department of Aerospace Engineering, University of Bristol, Bristol, BS8 1TR, UK.

Summary: The use of novel wing internal structure to control and improve aeroelastic (static shape, flutter / divergence and gust response) wing performance was investigated. Rib and spar variable orientation and crenellation concepts were explored making use of NASTRAN Finite Element and MATLAB tools developed as part of the work. The report focuses on the spar/rib arrangement and the crenellated skin concepts. It was shown how it is possible to increase the flutter speed and also reduce gust loads via these non-conventional structural configurations. An experimental investigation examined the behavior of 3D printed wings in a series of wind-off and wind-on experiments, and whilst the general behavior validated the numerical predictions, there was a significant scatter on the results. Further tests of coupons showed that the repeatability of the 3D printed materials is rather variable, and in particular, the direction in which the test pieces are manufactured has a significant influence upon the material properties.

TABLE OF CONTENTS

[1] Royal Academy of Engineering Airbus Sir George White Professor of Aerospace Engineering, AFAIAA.
[2] PhD Research Student

DISTRIBUTION A. Approved for public release: distribution unlimited.

1 Introduction, Concepts Explored & Report Scope

1.1 Introduction

Today's commercial aviation is predicted to see a growth of 5% per annum until at least 2030[1]. Such a promising future nonetheless faces some issues among which the industry's fossil fuel dependency is one of the biggest. The improvement in engine fuel efficiency has started to flatten, forcing aircraft designers to find efficiency improvement by focusing on the two other possibilities provided by the Bregeut equation - reducing weight and drag. This goal requires future aircraft to be optimised and designed with rules where traditional approaches may have to be changed.

The science of aeroelasticity focuses on the excitation and deformation of a structure under the interaction of elastic, aerodynamic and inertial forces[2]. The aeroelastic performance of aircraft wings has been considered for many years in the design process as a certification requirement so as to avoid undesirable flutter/divergence behaviour or catastrophic failure during a gust encounter[2]. Hence the control of aeroelastic behaviour was limited to consideration after the initial wing design, often resulting in the addition of extra weight. Aeroelasticity also dictates the deformed shape of the wing in flight, affecting the drag produced by aircraft. Challenged with the need to improve aircraft efficiency, aeroelastic performances are becoming key design drivers so as to reduce the amount of structure used by the wing, for flutter/divergence and gust response control, and also by tailoring wing deformation during flight to reduce drag. Understanding the different methods by which aeroelastic performance can be controlled is therefore important to aircraft designers.

One such static approach is known as *aeroelastic tailoring* and has been primarily researched using composite materials coupling phenomenon achieved through control of anisotropic properties[3]. The use of coupling phenomenon through either stacking sequence optimisation[4]–[8] or novel tow-steering methods[9], [10] have shown large positive impact on the aeroelastic performance in research work. However, since the initial work in the early 1980s, the idea of aeroelastic tailoring has mainly been a research topic investigated on conventional structural designs[6], [7], and has not yet found its way onto current commercial aircraft designs.

In addition to aeroelastic tailoring through composite tailoring, aeroelastic performance can be improved through the use of novel wing structural designs. This has been highlighted by research in wing structural optimisation which encompasses: (1) topology optimization and (2) shape optimisation.

Finding the optimal number and shape of structural features is the aim of topology optimization [11]. Research work using the Solid Isotropic Material with Penalization (SIMP) [12] method or the Level Set [13]–[15] method have shown that significant improvement in aeroelastic tailoring can be achieved through the development of novel wing structures. In addition, Kolonay and Kobayashi [16] showed similar improvements in aeroelastic tailoring using a cellular division method to perform topology, shape and sizing optimization of a fighter aircraft wing box. However, aeroelastic tailoring achieved through topology optimization often discards conventional structural members such as spars, ribs and stringers and generates complex solutions often hardly transferable into real designs.

An alternative approach is to use shape optimization to find the most advantageous structural members shape and arrangement for a wing box composed of conventional structural members e.g. spars, ribs and stringers. The use of the angles between the spars and the ribs to modify the bend-twist coupling of a wing was first shown by Harmin *et al.* [17] on an aluminium wing, where it was demonstrated that the change in bend-twist coupling could increase the flutter speed of a wing.

When considering structural members shape optimization, Vio and Fitzpatrick [18] and Vio *et al.* [19] showed that the use of curved spars and ribs can lead to significant increase in flutter/divergence speed and in reducing the root bending moment during a gust encounter. This research applied the concept of curvilinear spars and ribs using fixed nodes attaching the ribs and spars and so using a large design freedom. Locatelli *et al.* [20], Liu *et al.* [21], [22] have used curved spars and ribs to perform wing weight optimization subject to stress, buckling and aeroelastic flutter constraints on complex wing design. In their work, the spars and ribs curvatures were decoupled from the rib/spar arrangement. Such an approach was later taken by Jutte *et al.* [10] to show that aeroelastic properties could be impacted

DISTRIBUTION A. Approved for public release: distribution unlimited.

positively through the use of curved spars and ribs. Preliminary studies [17] on the use of the internal structure on metallic wings for aeroelastic tailoring have shown that improvements in flutter speed and gust response can be made through the variation of the skin thickness along the wing – a concept known as crenelated skins as shown schematically in Figure 2.

This report describes work undertaken to model aeroelastically, and validate experimentally, the impact on the static and dynamic aeroelastic behavior of simple wind tunnel test model wings using the following three concepts: the orientation between the ribs and spars, crenelated skins and curvilinear structures. An understanding was developed for the advantages of the different concepts compared to traditional configurations. Experiments were performed in the dynamics laboratory and wind tunnel in order to validate the analytical predictions. Further investigations were made to investigate the effect of the manufacturing process on the material properties of the test coupons.

1.2 Concepts Explored

1.2.1 Rib/Spar Arrangement

Classic structural design textbooks [23] limit the rib/spar arrangement on swept wings to only two cases: (1) the ribs perpendicular to the spars or (2) the ribs parallel to the air flow. Both of those orientations are shown in Figure 1. Although both arrangements are mentioned in design textbooks the second arrangement is often disregarded because of weight concerns and no consideration is made for aeroleasticity. The impact of the rib/spar arrangement was first explored by Harmin *et al.* [17] who highlighted that rib/spar arrangement impacted the wing bend-twist coupling and hence its aeroelastic performance. Here, these initial studies are further investigated and validated experimentally.

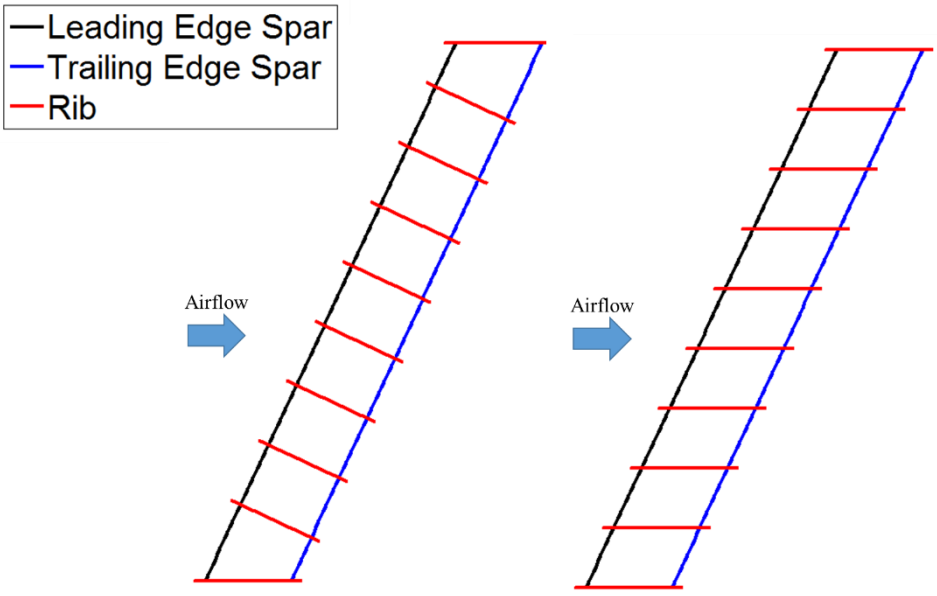

Figure 1. Design Textbook Rib Orientation for a Swept Back Wing.

1.2.2 Crenellated Skins

A crenelated skin is a skin of periodically varying thicknesses in, primarily, the span wise direction as shown in Figure 2. In this research, the following variables are used to assess the impact of the crenelated skin concept: (1) number of crenellations, (2) thickness of crenellations and (3) orientation of the crenellation with respect to the leading edge spar. Although Harmin *et al.* [17] showed the impact of the number and the thickness of the crenellation with respect to the orientation with the leading edge spar, a key difference with our work is the combination of crenellation and rib orientation. As such, we

consider crenellations and ribs where both have a similar orientation. Additionally the crenellations are placed only between the two spars.

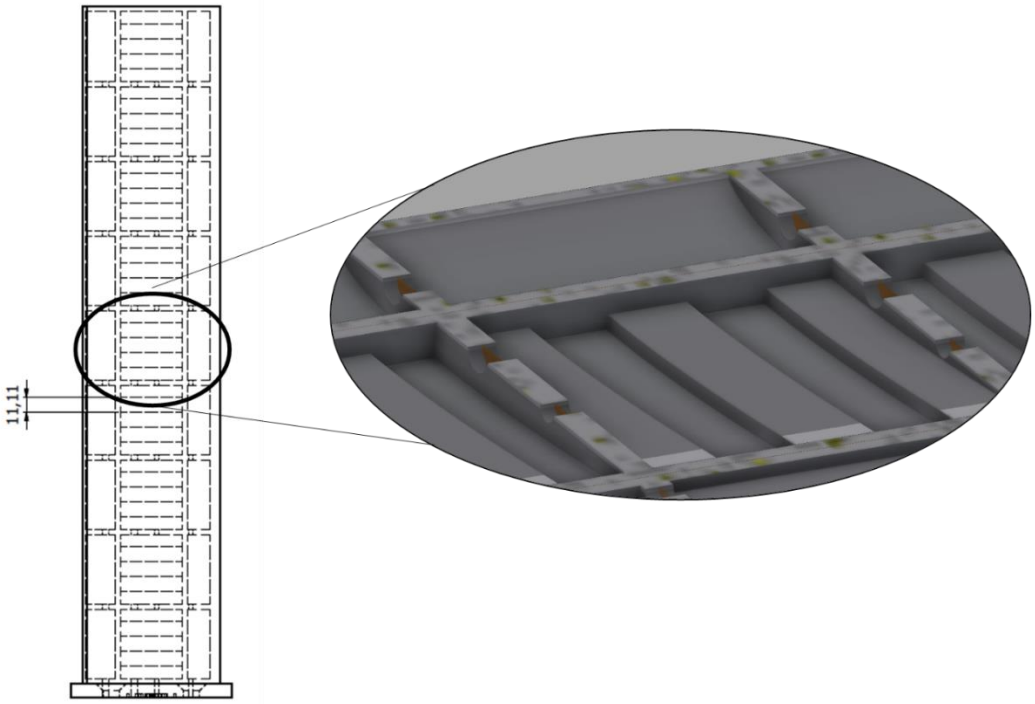

Figure 2. Illustration of a Crenelated Skin between the Spars on Straight Wing. Dimensions are in mm.

1.2.3 Curvilinear Structures

The final concept explored is the curvilinear structure which exploits curved spars, ribs and/or stringers as illustrated by Figure 3. The decision variable set offered by such concept is large, hence requiring the use of an optimization method to find quickly the most relevant structural shapes. It should be noted that this concept not only changes the shape of the wing structural components, but also changes the structural arrangement of the wing.

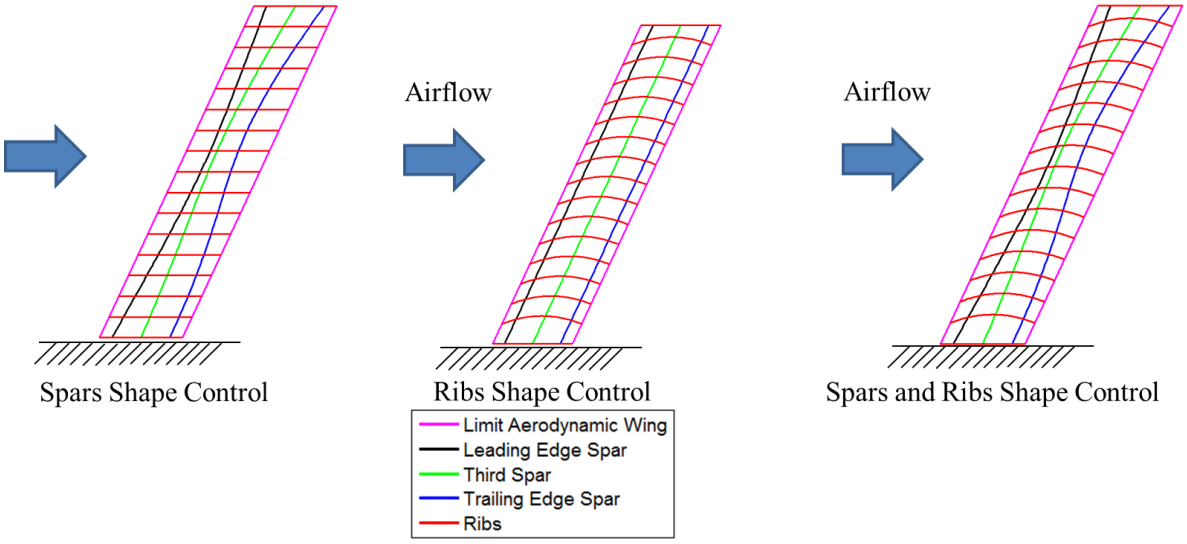

Figure 3. Illustration of the Different the Curvilinear Structure Concept.

DISTRIBUTION A. Approved for public release: distribution unlimited.

1.3 Report Scope

This report only considered the rib/spar arrangement and the crenellated skin concepts as both modelling and experimental work were performed for these two concepts. Experimental variations and errors, discussed later in this report, have up to now prevented the use of the curvilinear structure concept in the experiments.

2 Wing Geometry, Finite Element Modelling & Optimization Framework

2.1 Wing Geometry

The wing dimensions and the rib/crenellation orientation sign convention are shown on Figure 4, the wing geometry is untapered and un-swept with a span of 500mm and a chord of 100mm. The skin and spar/rib thickness are 2mm and 4mm respectively. The wing's internal structure consisted of 8 ribs, 2 spars and a root and tip ribs. The leading and trailing edge spar were placed at 25% and 75% of the wing chord, respectively. So as to avoid an increase in the skin panel size the change in rib/crenellation orientation created a half rib at each end of the wing. It should be noted that no crenellations were placed between the half rib and the tip/root rib introduced when the rib/orientation changed from the stream-wise position. Hence, changing the rib/crenellation orientation away from the stream-wise position moved the first crenellation away from the root (in contact to the half-rib at the root). Additionally, the introduction of crenellations on the skin did not move the position of the ribs - the rib spacing was maintained constant at the mid-chord position (56.56mm). Finally, it should be noticed that no attempt to balance the mass increase due the addition of crenellations/ribs was made, in this work as opposed to work done by Harmin *et al*. (2011), because of manufacturing tolerances.

Two different wing models were used: (1) a wing with a NACA 0012 aerofoil profile and of constant thicknesses for the spars and ribs and (2) a rectangular wing box with a constant thickness to chord ratio of 9.5% and of constant thicknesses for the spars and ribs. The constant thickness to chord ratio of the rectangular wing box was approximated by assuming thin-wall beam theory and considering the second moment of area contribution of the different structural members of the profiled wing section such that

$$h = \sqrt{\frac{\sum h_i^2}{n}} \tag{1}$$

where, h is the equivalent rectangular wing box height, h_i is the actual height of element i on the NACA profile wing box and n is the number of element considered. In this case only the two spars were considered as the spars height are the main differences between the rectangular wing box and the profiled wing section.

The dimensions of the different crenellated skins modelled are summarized in Table 1 and apply for all rectangular wing boxes considered in this report. The first crenellation is always after the root rib in the case of the 0^o rib/crenellation orientation and after the root half rib in all other cases. NACA profiled wing were made with no crenellations and crenellations with width 11.11mm and thickness of 4mm to match experimentally tested wings.

For the experimental part of this research only the aerofoil profiled wing model was used. The rib/crenellation orientation is indicated with respect to the incoming air flow and a positive orientation indicates the rib/crenellation leading edge are pointing towards the root.

DISTRIBUTION A. Approved for public release: distribution unlimited.

Table 1 Dimensions of crenellations modelled.

Crenellation Width (mm)	Total Number of Crenellations	Number of Crenellations per rib bay	Thickness Increase due to Crenellations	Thickness of Skin at the Crenellations (mm)
6.17	41	4-5	2	4
7.94	32	3-4	2	4
11.11	23	2-3	1.5	3
11.11	23	2-3	2	4
11.11	23	2-3	2.5	5
18.52	14	1-2	2	4
27.78	9	1	2	4

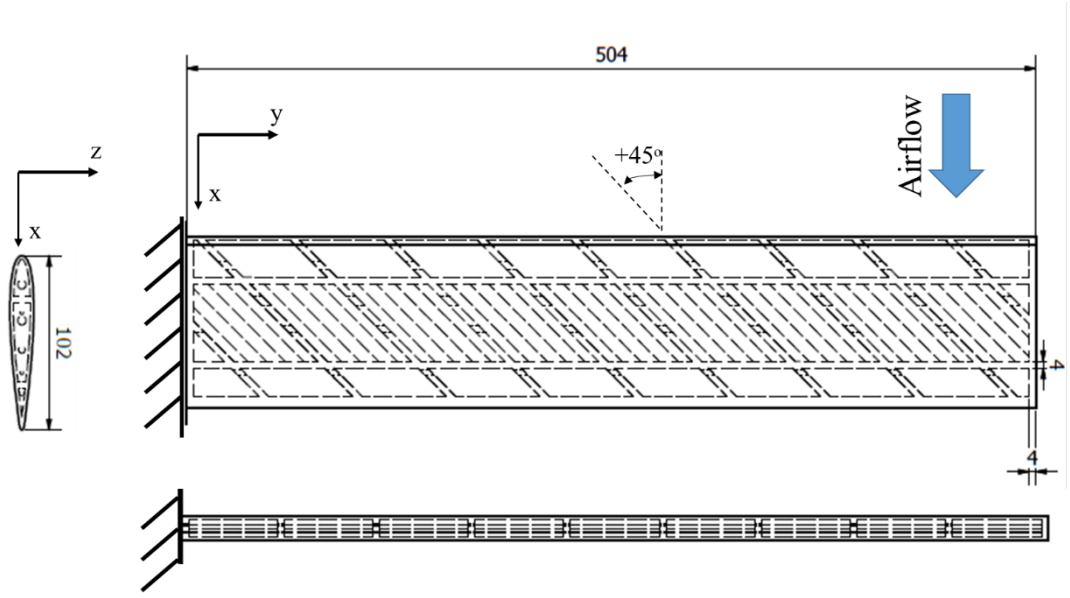

Figure 4. Wing model external dimensions in mm, rib/crenellation orientation and axis convention

2.2 Finite Element Modelling

Modelling of the different wing designs considered was performed using Finite Element (FE) analysis (NASTRAN). The geometry and the actions needed to create the different wing models were specified in a MSC.PATRAN session file by a MATLAB script; this session file was then read by MSC.PATRAN. Actions include the creation of the surfaces, meshing of the surfaces, node equivalence and check of the element geometries as well as the creation of element properties and boundary conditions to be used in the different analyses. IsoMesh and the Paver meshing algorithm were used to mesh the wing models. The structural model was made using 2D shell elements; initially, quadrilateral shell elements (CQUAD4) were used; however, these were replaced by triangular shell elements (CTRIA3) if the skew angle of the CQUAD4 elements was less than 30° using the MSC.PATRAN mesh verification tool. It should be noted that in the case of the NACA profiled wing, the FE model made no simplification about the wing geometry, and so the curvature of the NACA aerofoil were fully considered and so required a high number of elements. The NACA profiled FE model mesh contained over 120,000 structural elements and 900 aerodynamic panels for the aeroelastic calculations. The rectangular wing box models used contained over 50,000 structural elements. The mesh convergence of the different models used was checked for the different structural performance of interest.

DISTRIBUTION A. Approved for public release: distribution unlimited.

The FE wing models created using MSC.PATRAN had covers of constant thickness. The variation in thickness needed to model a crenellated skin was implemented though a MATLAB script. The orientation of the thickness axis (z axis) for every element was verified to be similar for all elements in MSC.PATRAN. The increase in skin thickness and a change in offset values for the 2D shell elements on the top and bottom skin making the thick region of the crenellation were made using a MATLAB script, ensuring that the crenellations were inside the wing box and that the outside skin was flat, as seen on Figure 5.

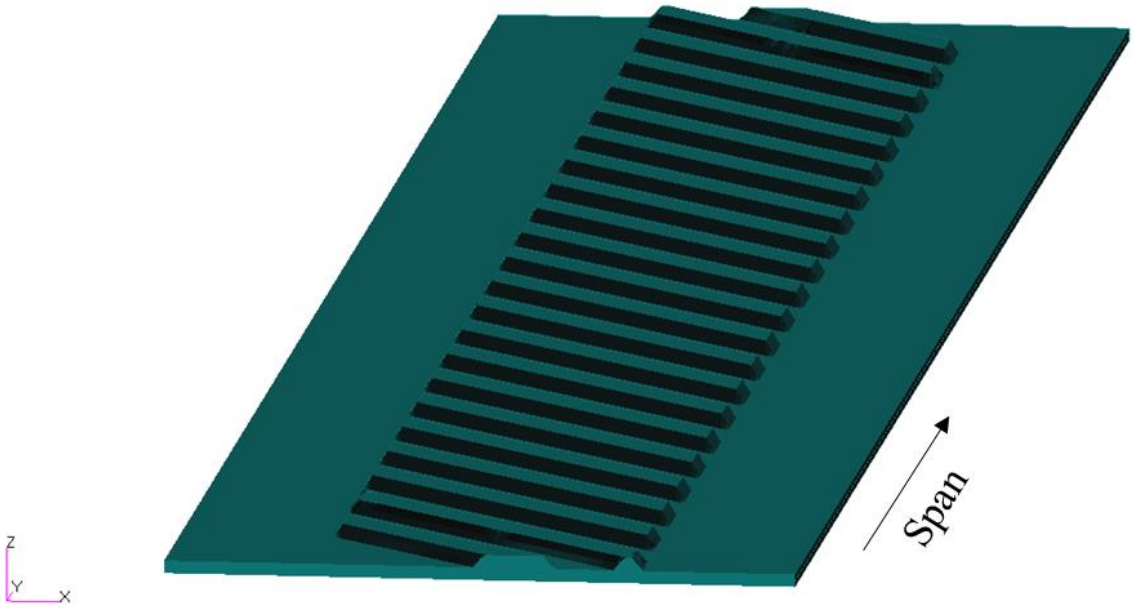

Figure 5. FE model of a crenellated skin displaying shell thicknesses for a rectangular wing box

2.3 Curved Structure Parametrisation

The wing structural member's position and shapes are controlled using Bezier curves - a polynomial representation method often used in optimisation methods as it allows the control of the polynomial curves with only a limited number of control points. The polynomial curve is strictly defined by the control points thus limiting the number of decision variables making it an attractive method for optimisation purposes[24]. The Bezier curve representation can be expressed using the generalised formula shown in Equation 1 where the position of the control points permit the development of a polynomial equation used for shape parametrisation with n the number of control points, $\overline{P}_i$ the control points and $B_{i,p}(u)$ p order Bernstein polynomials.

$$\overline{R}_g(u) = \sum_{i=1}^{n} \overline{P}_i B_{i,p}(u) \tag{2}$$

The number of control points (n) is of $p + 1$ for a shape polynomial of order p. In this work, only second and third order curves where used. For such purposes Equation 1 can be expressed in an explicit form shown in Equation 3, where t represents the number of points on the curve and P_i the control points coordinates.

$$B(t) = \sum_{i=0}^{n} \binom{n}{i} (1-t)^{n-i} t^i P_i \qquad (3)$$

Using Equation 3 in two dimensions, a list of points ordinate and abscissa values defining the position and shape of the spars, ribs, crenellations and stringers is found. The depth direction for each point can be added by considering the profile of the wing box – a rectangle in this particular case. It should be noted that in the case of a wing with an aerofoil profile the equation describing the aerofoil profile is used to find the depth position of the different points.

3 Analysis Performed

3.1 Static analysis

To assess the impact of the crenellations on the wing deflection and twist, a static analysis (SOL 101) was performed for every wing design considered. The wings were assumed to be fully fixed at the root. A tip load was applied though a Multiple Point Constraint (MPC) slaving all the tip nodes to a node placed at the tip mid chord and at the middle of the wing depth. This loading condition generates a bending load and a torque for an aerofoil profiled wing. All FE analyses were performed using the highest load used during the experiment: 487g.

The static experiment reproduced the static loading modelled in FE. A series of loads were applied on the wing using the Load Application Device (LAD). The loads were 124, 245 and 487g; the use of three loads assured that no plastic deformation occurred during the test. The LAD consisted of a rectangular part with an opening of the shape of the wing aerofoil which is slightly larger than the wing aerofoil. The LAD was 1cm thick hence the tip deflection recorded during the experiment was offset by 1cm in board. The wings were bolted with four 12mm steel bolts to a bench to assure a fully fixed boundary conditions. A 5M pixel cameras 3D Dantec Q400 Digital Image Correlation (DIC) system – a contactless displacement measurement method - was used to measure wing deflections. The DIC cameras were placed above the wings and recorded the whole of the top side deflections. The set up for the static testing is shown in Figure 7. For every test point, a DIC image was captured after 10min under load. The experiment was repeated three times for the wings with rib/crenellation orientation of 0^o and 30^o, and four times for all other wings.

Secondly, the position of the Flexural Axis was estimated for the wing boxes in FE modelling by applying a unit load at the leading and trailing edge at various sections along the wing models. This analysis assumed that the flexural axis is the line connecting flexural centres which are a point on a wing section at which the application of a shear force creates no twist of that section with respect to the root [26], [27].

3.2 Modal analysis

The natural frequencies of the different mode shape of the wings were estimated using modal analysis (MSC. NASTRAN SOL 103). These results were compared with the experimental ones. The wing was, once again, assumed to be fully fixed at the root.

Dynamic testing was used to find the natural frequencies, damping ratios and the associated mode shapes. A “hammer” test was performed using a single accelerometer placed at the tip of the wing and impacting the structure at various impact points as shown by Figure 6 using five averages. The data measurement and analysis was performed using LMS International software.

DISTRIBUTION A. Approved for public release: distribution unlimited.

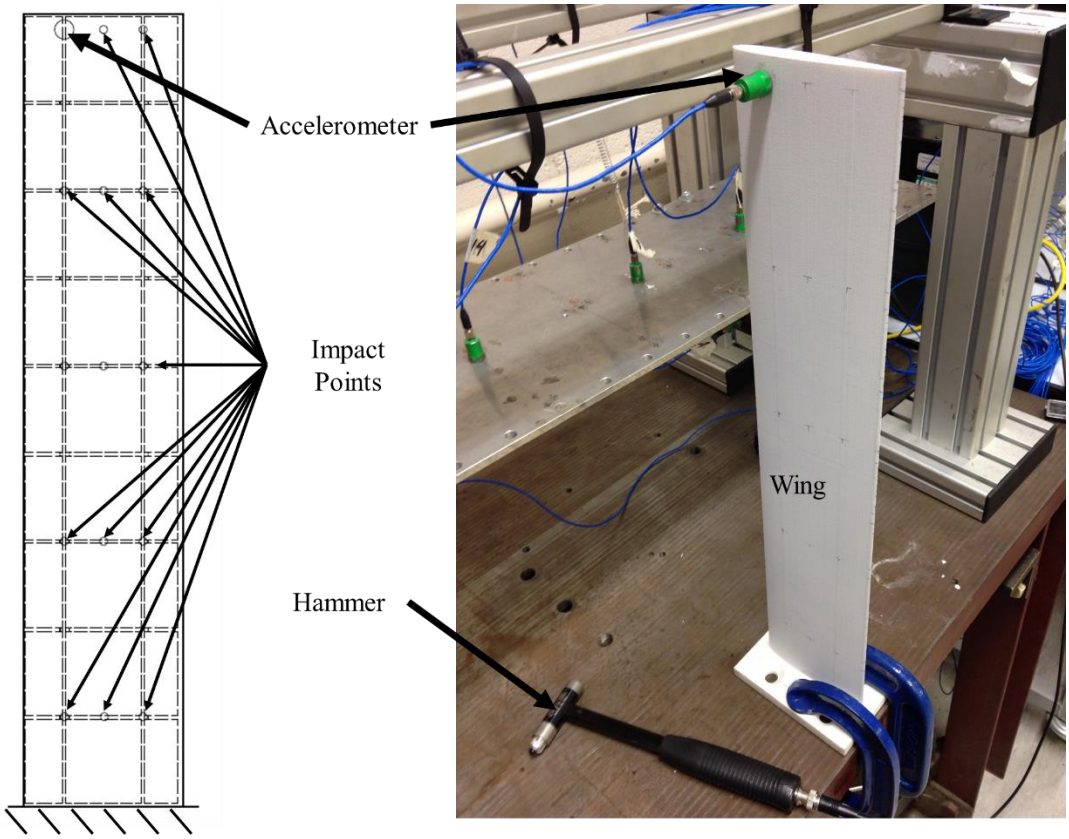

Figure 6. Accelerometer and impact locations and dynamic experiment set up.

3.3 Aeroelastic analysis

The static aeroelasticity analysis (MSC.NASTRAN SOL 144) was performed at an angle of attack of 5° and at a speed of 35m/s using a doublet lattice panel method. The deflection and twist of the wing under different aeroelastic loading was assessed. In this analysis, the wing was assumed to be fully fixed at the root. This analysis was applied to both FE models. The modelling was performed at an air temperature of 25°C, similar to the temperature experienced in the wind tunnel. A symmetry at the root was assumed to consider the reflection from the wind tunnel wall [28].

To match the modelling conditions experimentally, the manufactured wings were placed horizontally in the low turbulence wind tunnel at the University of Bristol and fixed to one wall. The DIC camera was placed outside the wind tunnel looking at the underside of the wings through a glass wall to measure the deflection and twist of the wing. Due to distance restrictions only the tip end of the wing was in the field of view of the cameras. The wind tunnel set up is shown in Figure 7. The wings were fixed at an angle of attacks of 5° and the wind tunnel speed was set at 0, 25, 30 and 35m/s. At each test point, a DIC image was captured after 2min, 4min and 5min under load. A temperature variation of no more than 2°C was observed during the tests. The experiment was repeated three times for every wing.

DISTRIBUTION A. Approved for public release: distribution unlimited.

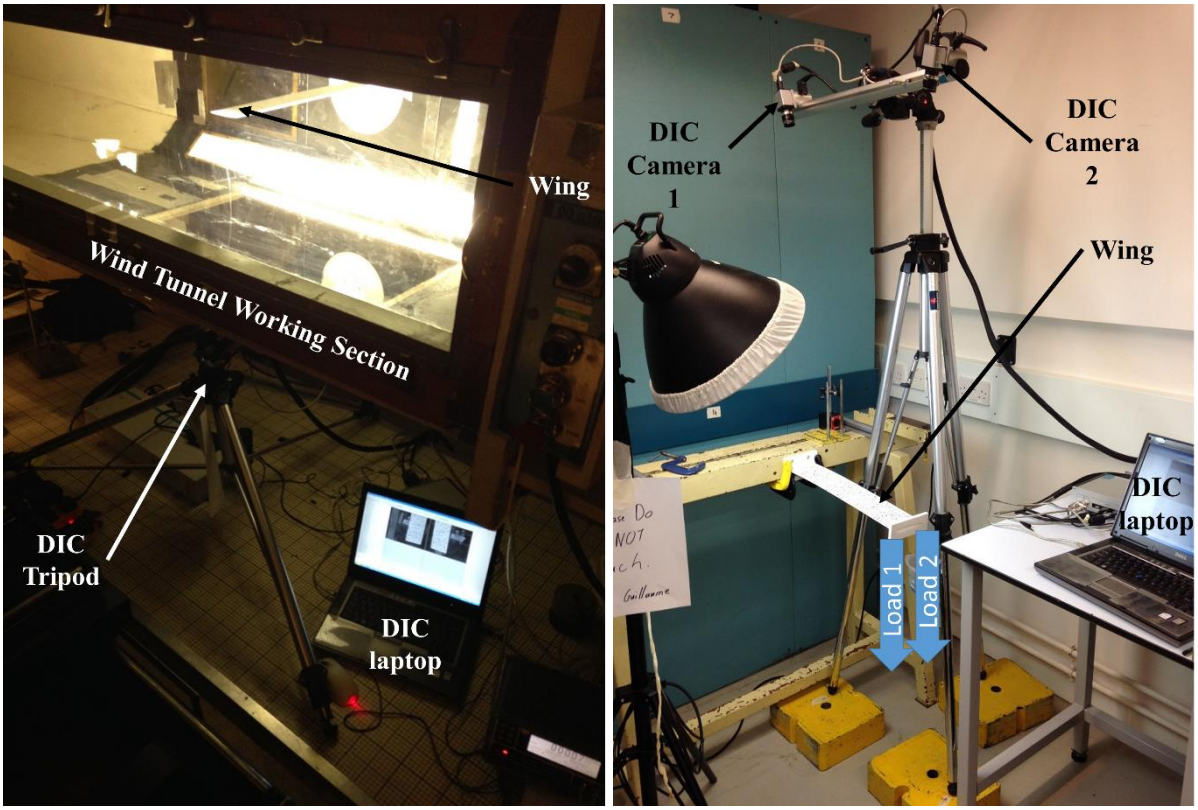

(a) Wind tunnel experimental set-up (b) Static testing experimental set-up

Figure 7. Experiment Set-Up

3.4 Gust analysis

Gust loads can be of crucial importance to aircraft designer as they can be the design loads for which the wing structure is sized. It is, therefore, important to assess the impact of the crenellation concept on gust loads. Various metrics can be used to assess this impact as explained in [29]. Considering that only the wing is considered and is assumed to be fully fixed during the analysis, the root bending moment generated during a gust encounter was chosen as the metric of interest.

Gust events are simulated assuming the gust velocity profile varies as '1-Cosine' using MSC.NASTRAN SOL 146 for which the time domain gust velocity is expressed using

$$w_g(T) = \frac{w_{g0}}{2}\left(1 - \cos\frac{2V\pi}{L_g}T\right) \tag{14}$$

with T the analysis time variable, w_g, the peak gust velocity and the gust length L_g [2]. The gust analysis was performed at sea level and at a speed of 35m/s at 25°C. A symmetry at the root was assumed to model the reflection from the wind tunnel wall [28]. A value of 0.5% of structural damping was used in this analysis. Six gust lengths were considered varying linearly from 0.7m/s to 7.0m/s with a peak gust velocity of 0.5m/s. The wing root is assumed to be fully fixed through a Multiple Point Constraint (MPC). The wing root bending moment was assessed by considering the bending moment created on the node slaving all the nodes at the root. The maximum root bending moment for a given wing design was found by fitting the root bending moments at each gust length using a Radial Basis Function (RBF) [29] method.

3.5 Aeroelastic instability speed analysis

The aeroelastic instability speed analysis was performed using MSC.NASTRAN PKNL analysis (SOL 145). The PKNL method is a PK method that uses direct matching of air speed, Mach number

DISTRIBUTION A. Approved for public release: distribution unlimited.

and air density at which to investigate the behaviour of the wing [28], [30]. The analysis was performed with a range of Mach number from 0.01 to 0.5 with matching airspeed at sea level and at 25°C using a doublet lattice panel method. A symmetry at the root was assumed to consider the reflection from the wind tunnel wall [28]. The first aeroelastic instability was found by tracking sign inversion in the mode damping values. The inclusion of 0.7% of structural damping prevented the triggering of soft flutter modes in the analysis [2], [28].

4 Preliminary Study on a Rectangular Wing Box using FE

4.1 Mass Analysis

The crenellation scheme introduces the crenellated skin concept by locally increasing the skin thickness. This scheme makes no alteration to the rest of the wing box structure thicknesses. Thus the introduction of crenellations on the wing leads to an increase in the wing mass due to an increase in material on the wing as shown by Figure 8 and Figure 9.

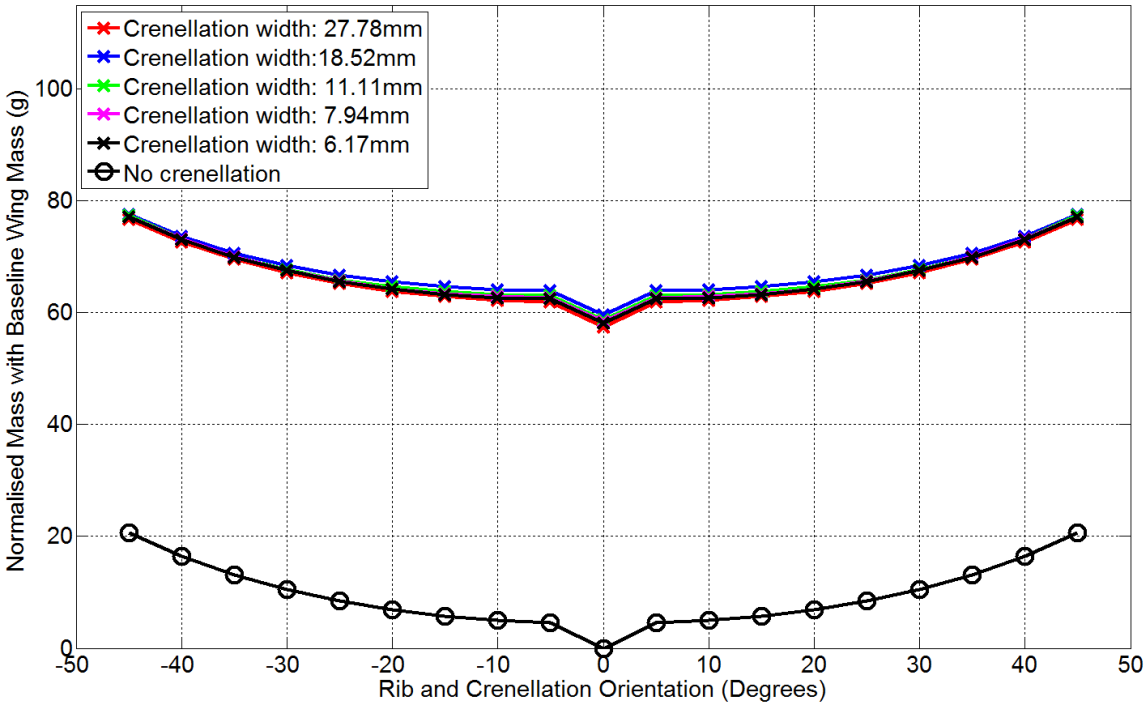

Figure 8. Wing mass variation for different crenellations width and rib/crenellation orientation.

DISTRIBUTION A. Approved for public release: distribution unlimited.

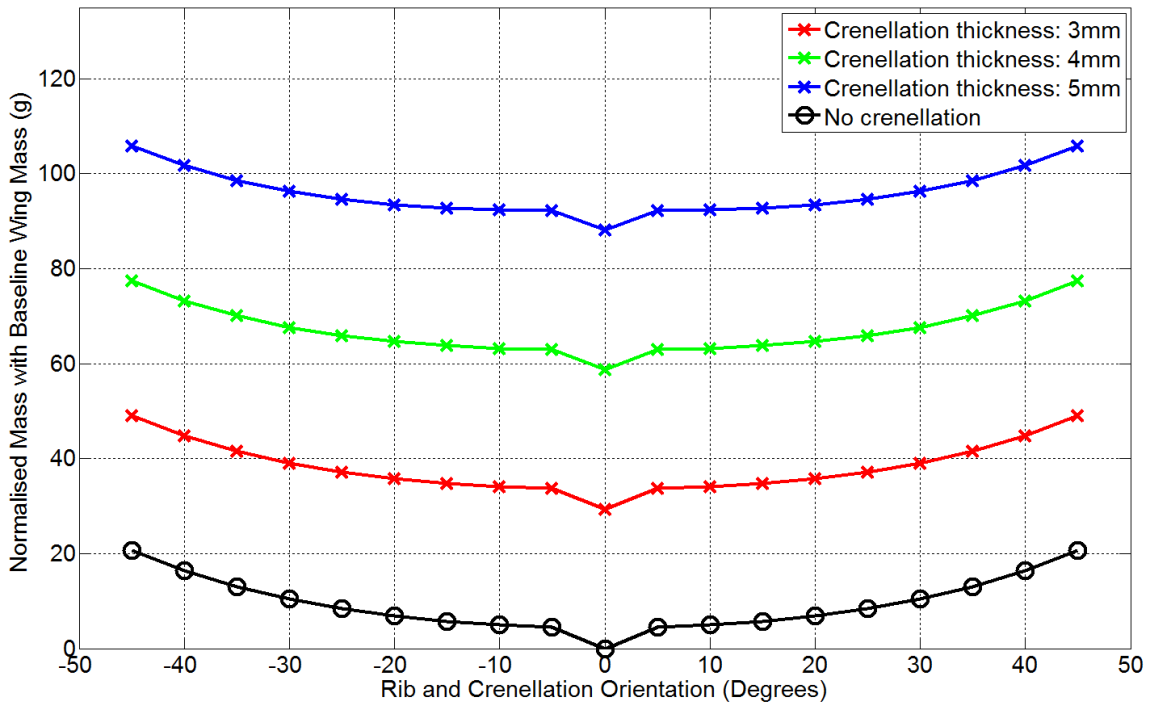

Figure 9. Wing mass variation for different crenellations thickness and rib/crenellation orientation.

4.2 Static Analysis

Figure 10 and Figure 11 show the average tip displacement and tip twist obtained by FE analysis, for various crenellation widths and rib/crenellation orientations on a rectangular wing

It can be seen that the change in rib orientation - when no crenellations exist - creates a small variation in tip displacement and alteration in tip twist. The tip displacement first increases with the increase of rib orientation and then decreases once the rib orientation is above 25°. Above this value the ribs change their structural behaviour and increasingly act as spars – increasing the span-wise stiffness. The rib orientation can change the sign of the tip twist rotation and provide a cubic polynomial curve with two distinct stationary points where similar values of twist can be achieved with different rib orientations as shown by Figure 11.

The addition of crenellations creates a reduction of at least 3.7% in average tip displacement. This result increases as the crenellation gets wider, as explained by the thicker skin provided by the crenellations which increases the second moment of area of the wing and prevents wing deflection.

It is interesting to notice that the decrease in tip displacement due to an increase in crenellation width is non-linear. Increasing the crenellation width from 18.52mm to 27.78mm leads to reduction of 0.51% instead of 0.12% when increasing the crenellation width from 6.17mm to 7.94mm. This behaviour is due to the fact that the alteration between a thick and a normal thickness skin is dependent on the crenellation width. Hence, for example, the thicker crenellation widths have a higher initial second moment of area than the thinner one and keep their higher second moment of area for a longer initial wing section.

Figure 10 shows that the trends in average tip displacement variation with the rib/crenellation orientation is similar to the one observed with changing just the rib orientation for all the crenellation widths considered except the widest crenellation. For the wings with crenellation width of 27.78mm the stiffening effect due to the rib/crenellation orientation is less than the one observed for other crenellations widths. Note that the widest crenellation concept is the only one with an identical number of crenellations for every rib bay as shown by Table 1 hence the centre of gravity of those wings are slightly offset from the mid-span location towards the tip. Thus the increase in material due to the change in rib/orientation does not follow the same pattern as the other concepts and explains the change in average tip displacement versus rib/crenellation orientation's trend.

DISTRIBUTION A. Approved for public release: distribution unlimited.

Interestingly, the addition of crenellation increases the tip twist especially when the crenellations are placed at high orientations. Overall, the addition of crenellation reduces the ordinate distance between the two stationary points of the cubic tip twist curve created by varying the rib orientations.

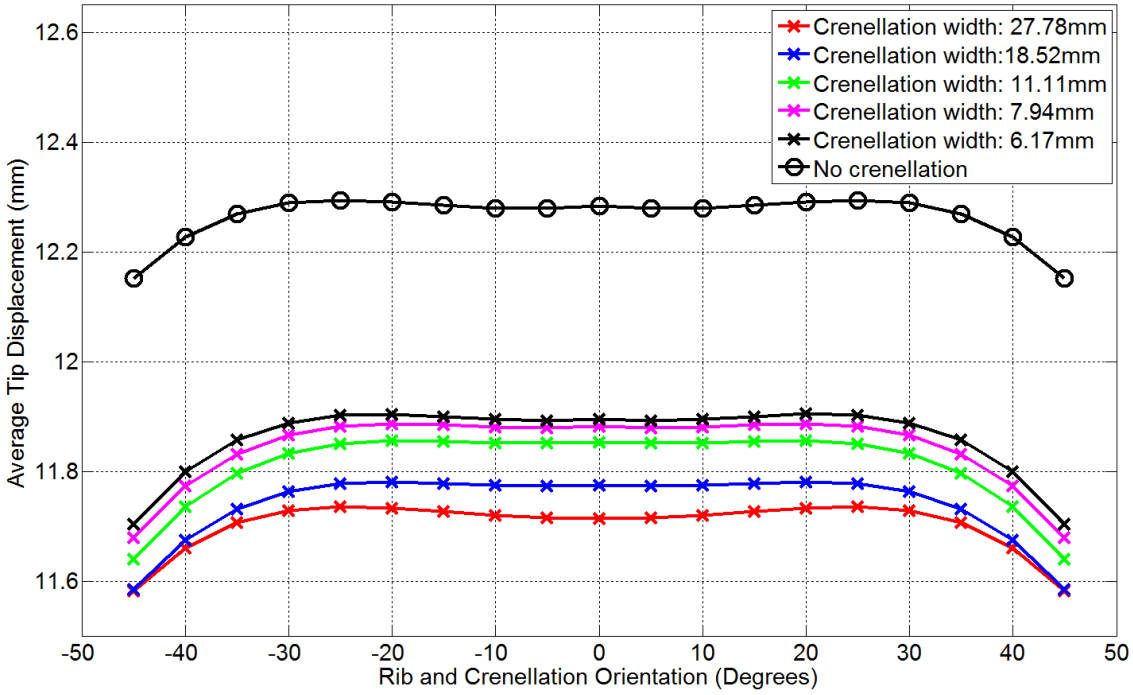

Figure 10. Average tip displacement for different crenellations width and rib/crenellation orientation on a rectangular wing box.

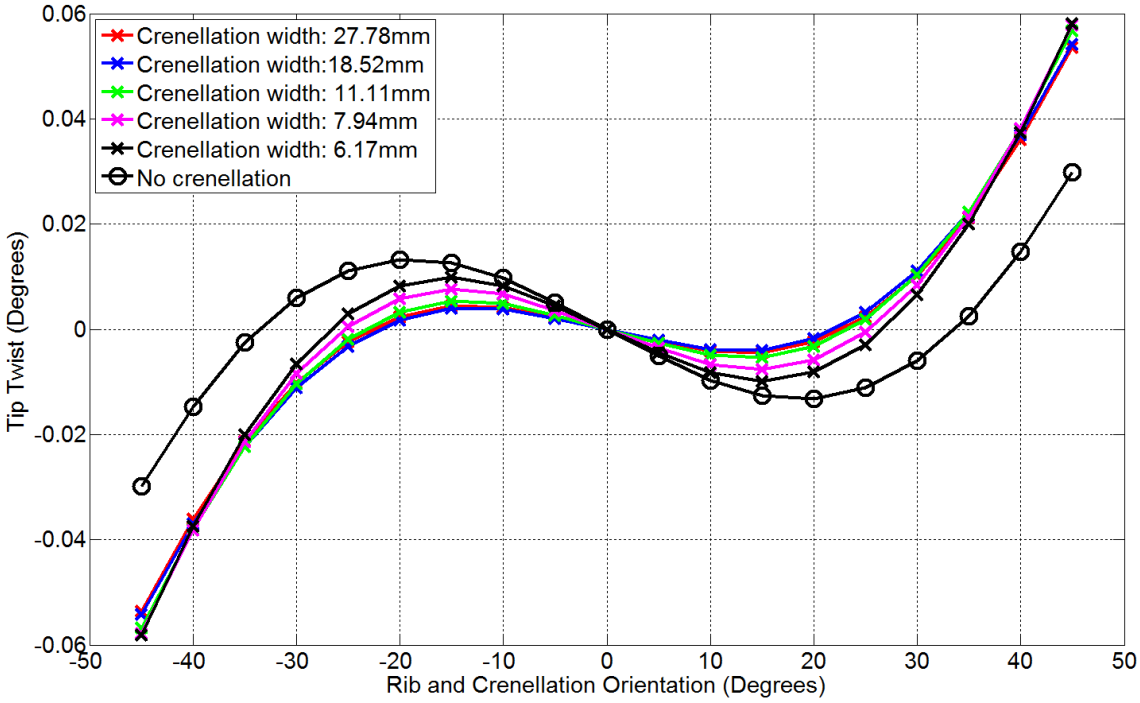

Figure 11. Tip twist for different crenellations width and rib/crenellation orientation on a rectangular wing box.

DISTRIBUTION A. Approved for public release: distribution unlimited.

Figure 12 and Figure 13 show the change in average tip displacement and tip twist for various crenellation thicknesses and rib/crenellation orientations. Clearly, when the crenellation thickness is increased the average tip deflection is reduced. This effect can be related to an increased second moment of area. The crenellation thickness has an interesting impact on the tip twist curves. The highest tip twist is achieved at high crenellation orientations and with a crenellation thickness of 4mm and this crenellation thickness also has the tip twist curve with the second lowest ordinate distance between stationary points. While a wing with a crenellation thickness of 5mm has the second highest twist and yet its tip twist curve is almost similar to the wing with no crenellation in the crenellation orientation range [-10°, 10°].

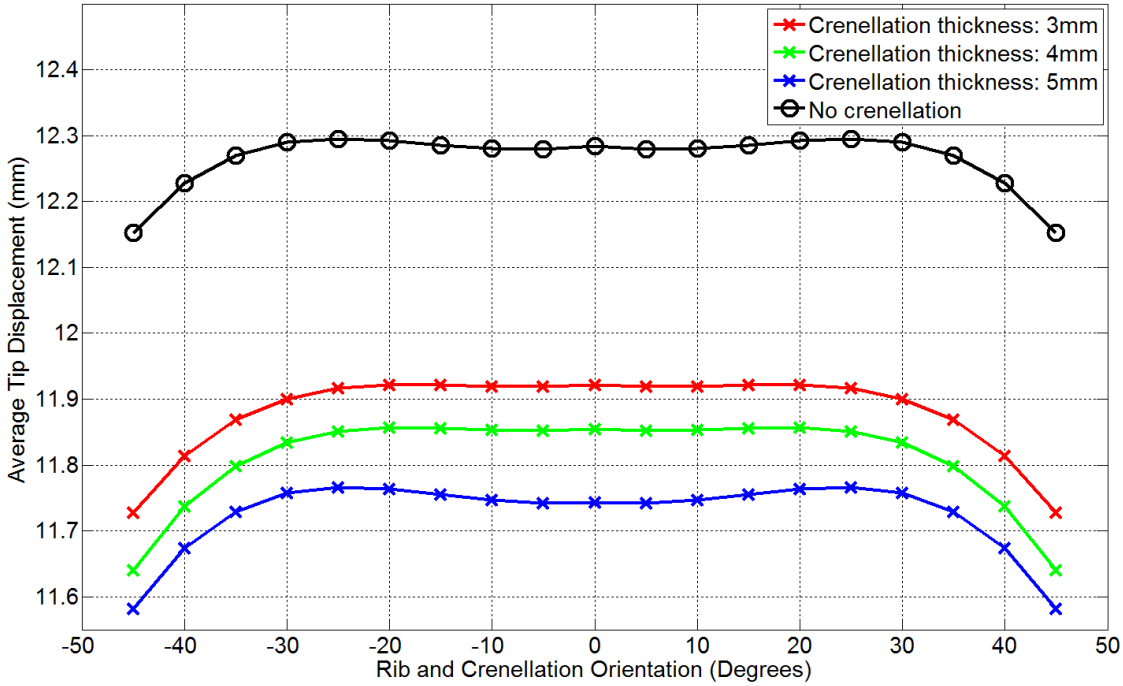

Figure 12. Average tip displacement for different crenellations thickness and rib/crenellation orientation on a rectangular wing box.

DISTRIBUTION A. Approved for public release: distribution unlimited.

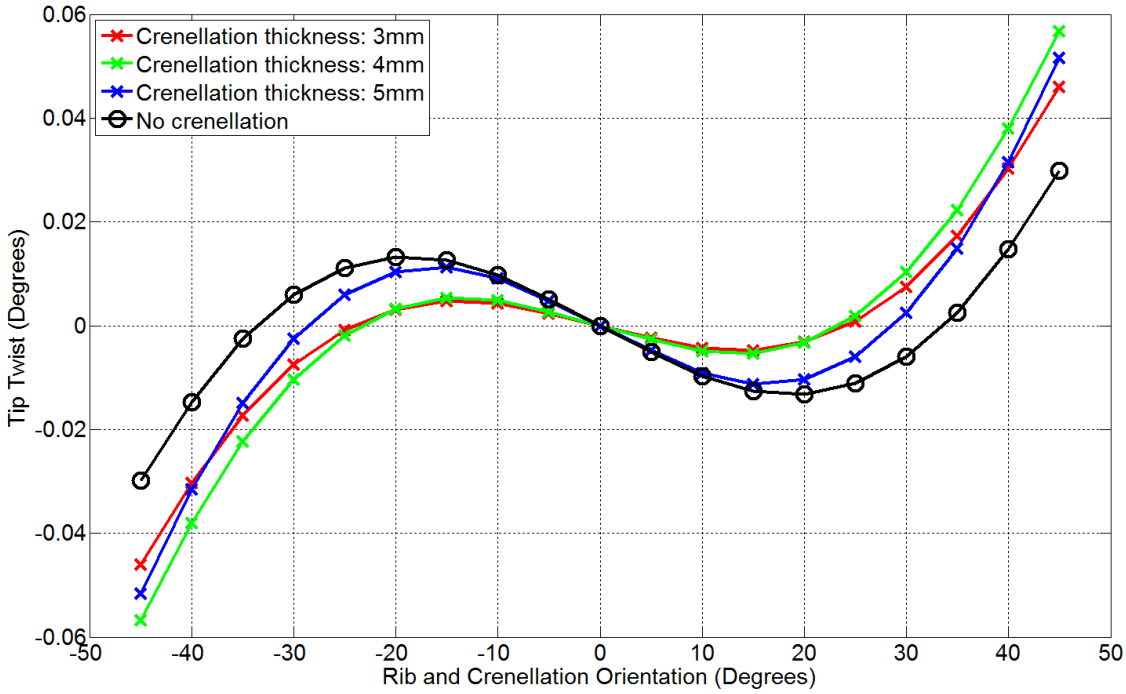

Figure 13. Tip Twist for different crenellations thickness and rib/crenellation orientation on a rectangular wing box.

4.3 Modal Analysis

Figure 14 and Figure 15 show the variation in the first four natural frequencies of the rectangular wing box model with different crenellation widths and thicknesses. The first four modes are: first bending, second bending, forward/aft and first torsion for all the wings considered except for eight wings. These wings have a rib orientation of ±45° and ±40°. Four wings have a crenellation width of 18.52mm and four have a crenellation thickness of 3mm. For those wings the order of the forward/aft and second bending mode swaps. It should be noticed that these two modes have very close natural frequencies (maximum difference 0.1%).

The addition of crenellations, the increase in the number of crenellations and the increase in the crenellation thickness reduce the first three natural frequencies of the wing. The addition of crenellations, the increase in the number of crenellations and the decrease in the crenellation thickness increase the fourth mode natural frequency highlighting the potential of crenellated skins for flutter control. The decrease of the bending modes natural frequencies can be related primarily to the increase in wing mass. For example, the addition of crenellations with width of 11.11mm and crenellations thickness of 4mm increases the wing mass by 17.7% while the wing bending stiffness only increases by 3.6%. The increase in torsion mode natural frequency is due to an increase in torsional rigidity due to the increase in thickness, dominating over the increase in mass moment of inertia.

Clearly, changing the rib/crenellation orientation impacts both the bending and torsion mode natural frequencies as the first bending and torsion mode natural frequencies reduces by up to 2.2% and increases by up 3.8% respectively due to a change in rib/crenellation orientation. This can be explained by the ability of the rib/crenellation orientation to primarily increase the wing mass and the torsional stiffness of the wing.

It should be noted the wings with crenellation width of 27.78mm display significantly different natural frequency values for the first three modes compared to other wings with crenellations. This result can be related to the fact that this crenellation width was found to introduce the least increase in mass as shown in Figure 8. Additionally, this crenellation concept has an offseted center of gravity towards the tip as the first and last rib bay have the same crenelated skin order with only one crenellation and one normal skin region.

DISTRIBUTION A. Approved for public release: distribution unlimited.

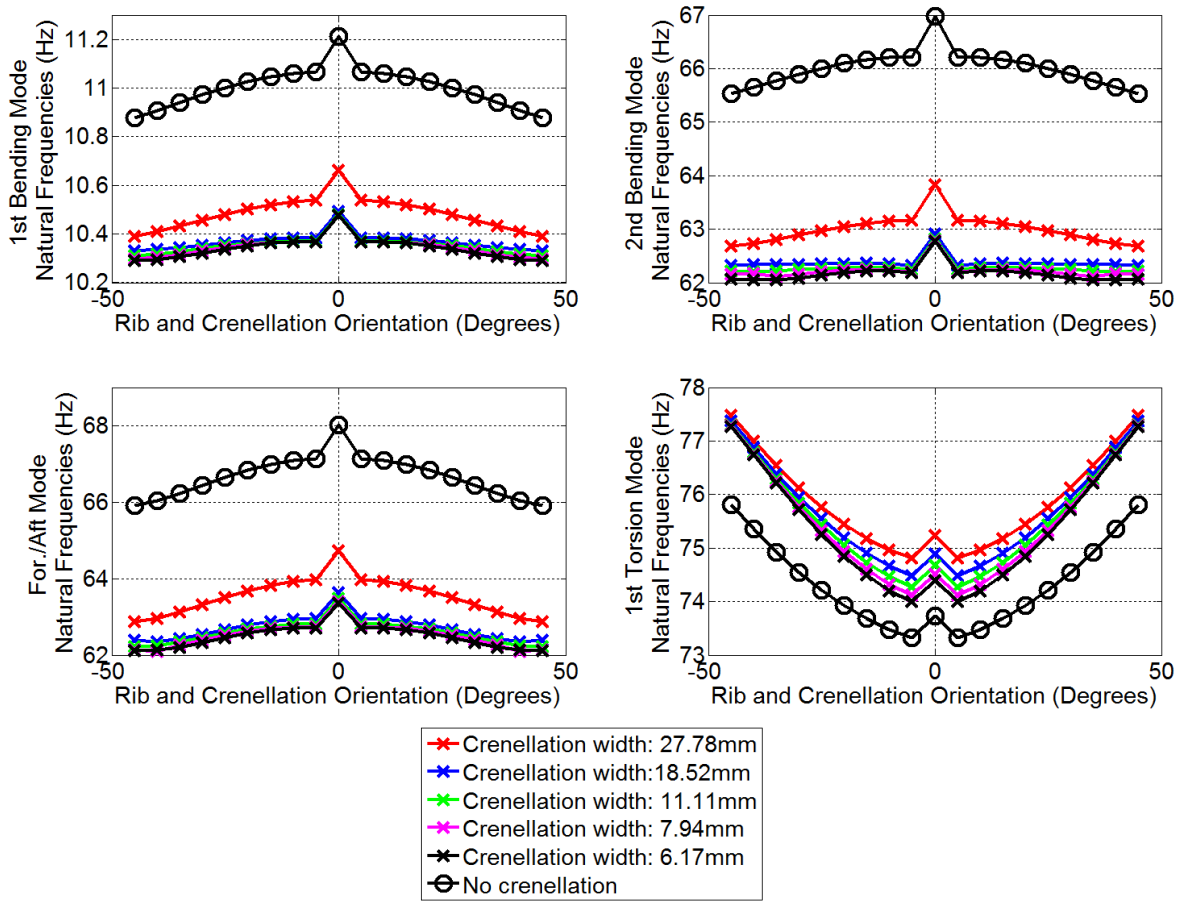

Figure 14. Variation of the first four natural frequency for wings with no crenellation and crenellation of different width and different rib/crenellation orientation on a rectangular wing box.

DISTRIBUTION A. Approved for public release: distribution unlimited.

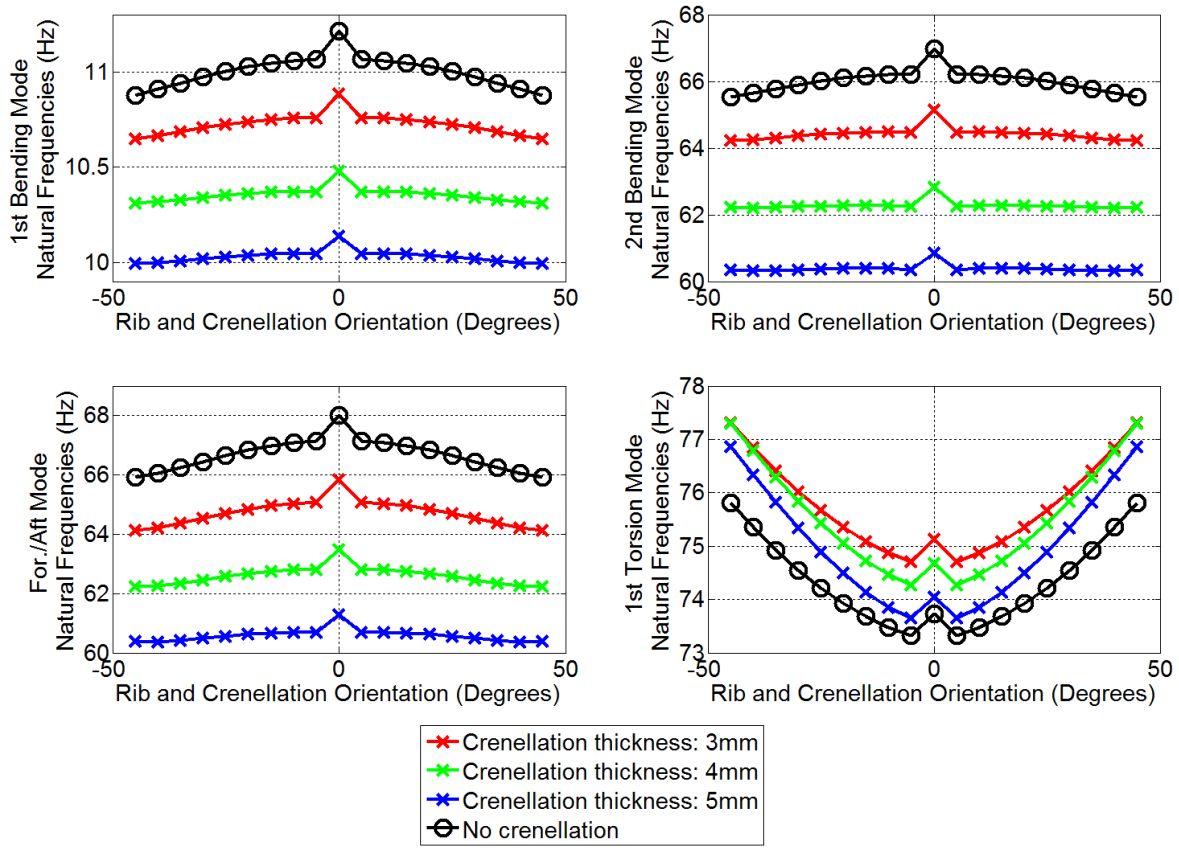

Figure 15. Variation of the first 4 natural frequency for wings with no crenellation and crenellation of different thickness and different rib/crenellation orientation on a rectangular wing box.

4.4 Static Aerodynamic Analysis

Figure 16 and Figure 17 show the average tip displacement and tip twist for various rectangular box wing designs with and without crenellations of different width and rib/crenellation orientations when subject to aerodynamic loading. Figure 18 and Figure 19 show the average tip displacement and tip twist for rectangular wing box designs of different crenellation thickness. These curves display similar trends to the ones presented in the static analysis except that the symmetry found by the 0° rib/crenellation orientation is suppressed.

The addition of crenellations, increasing the crenellation width and its thickness reduce the tip displacement and the nose up tip twist compared to the wing with no crenellation. Changing the rib/crenellation orientation leads to a reduction in tip displacement and a variation in nose up tip twist.

All wings experienced a nose-up tip twist and all the curves' trends seen on Figure 16-19 are reduced on the positive rib/crenellation orientation side compared to the curve variation seen in the static load case. The curves' trends are increased in the negative rib/crenellation orientation side.

The nose up tip twist experienced by all wings was expected as in this analysis a span-wise distributed load located around the quarter chord region is used. The movement of the load from the mid-chord position to the quarter chord region means that the load is always located in front of the flexural axis for every wing considered and so a nose-up twist appears.

The lack of symmetry by the 0° rib/crenellation orientation was expected as in this analysis the load varies with the twist distribution produced by the different wings under load. The movement of the load from the mid-chord position to the quarter chord region means that the load is applied closer to the wing flexural axis for wings with a high negative rib/crenellation orientation. Hence, the aerodynamic load produces less torque on such wings, and so less nose-up twist and so less load than the wings with a high positive rib/crenellation orientation.

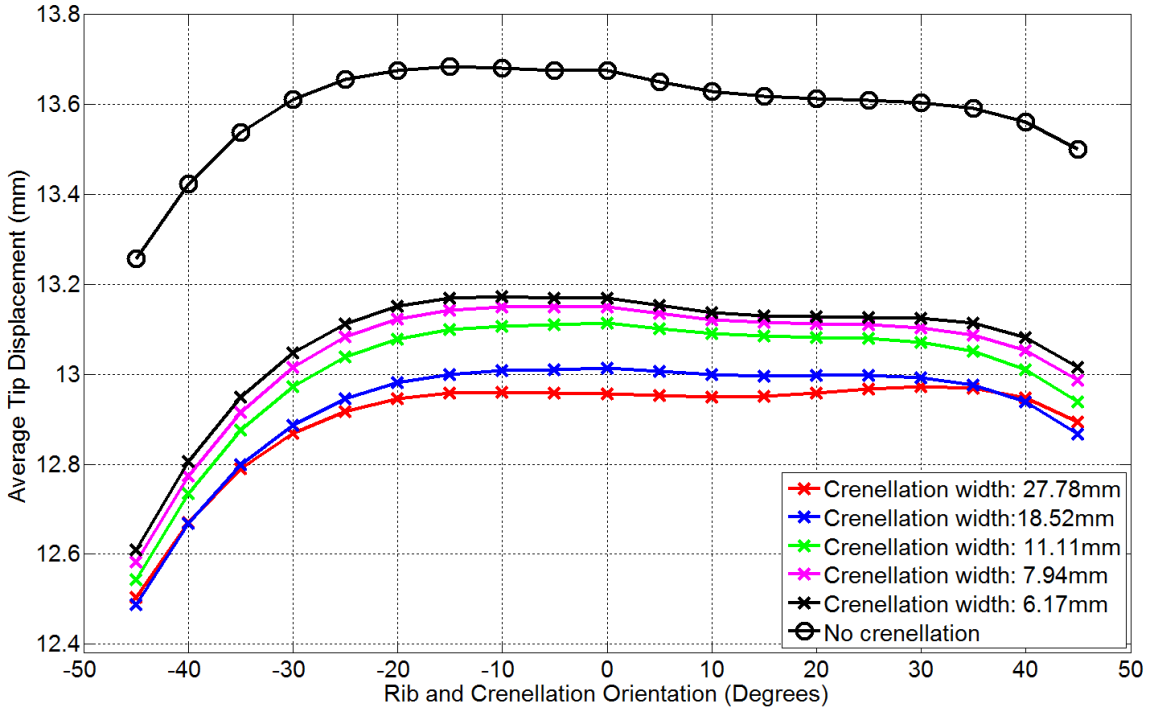

Figure 16. Average tip displacement for different crenellations width and rib/crenellation orientation on a rectangular wing box at an angle of attack of 5° and airspeed of 35m/s.

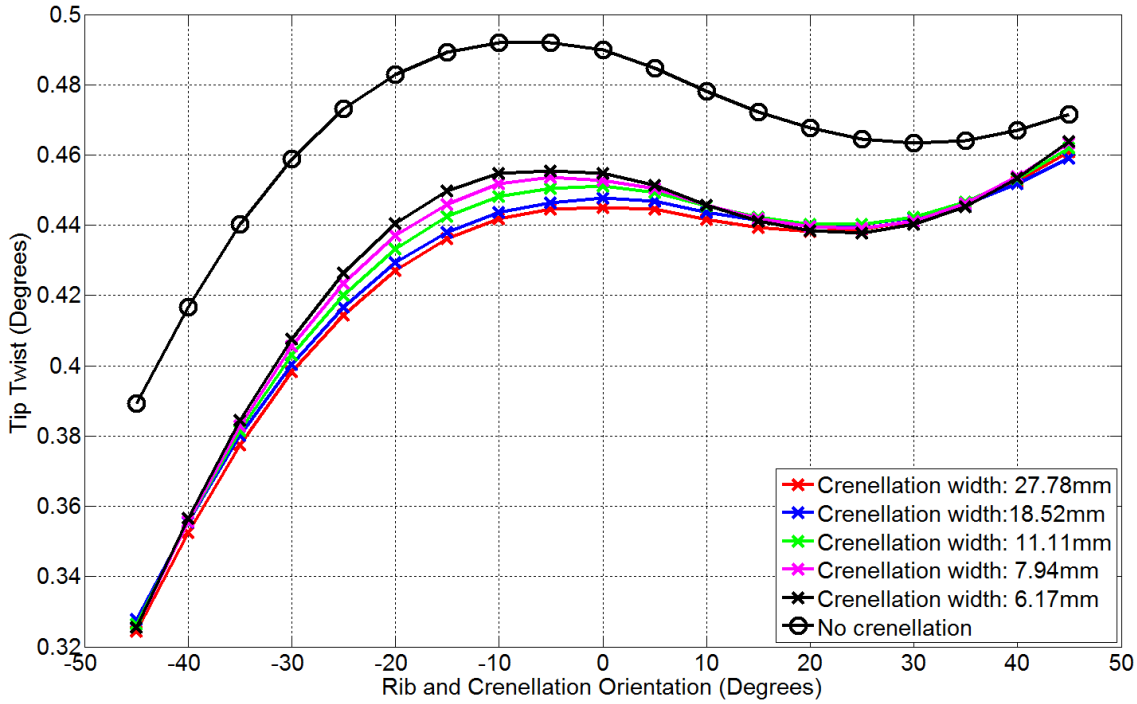

Figure 17. Tip twist for different crenellations width and rib/crenellation orientation on a rectangular wing box at an angle of attack of 5° and airspeed of 35m/s.

DISTRIBUTION A. Approved for public release: distribution unlimited.

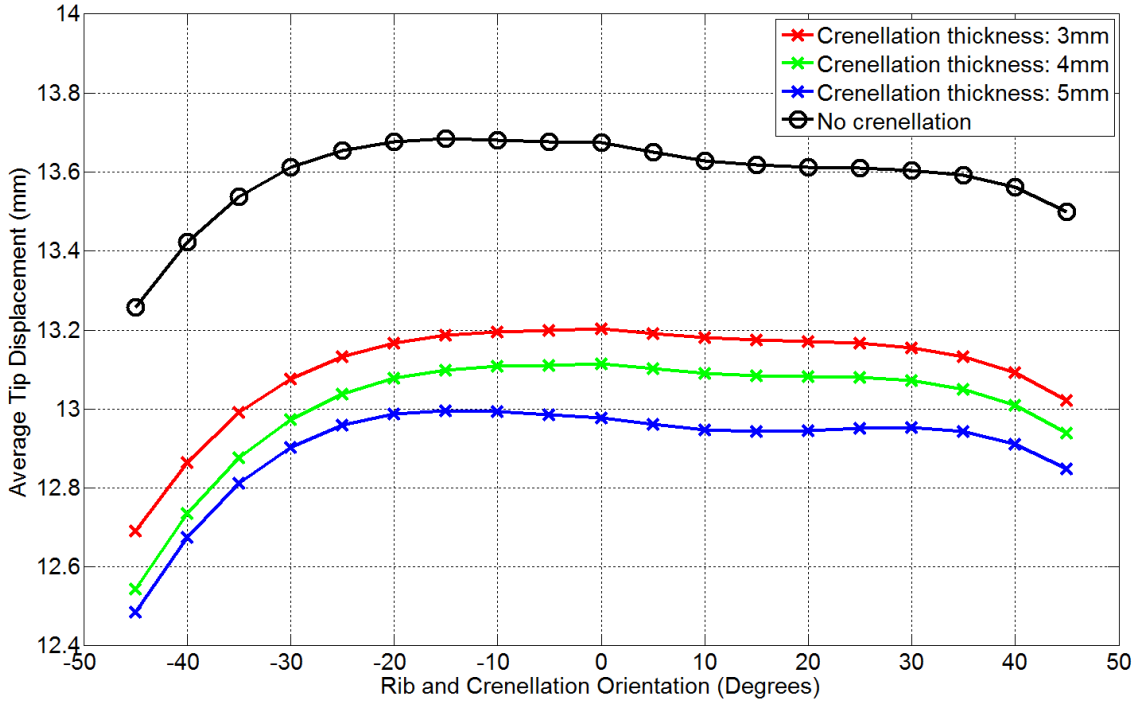

Figure 18. Average tip displacement for different crenellations thickness and rib/crenellation orientation on a rectangular wing box at an angle of attack of 5° and airspeed of 35m/s.

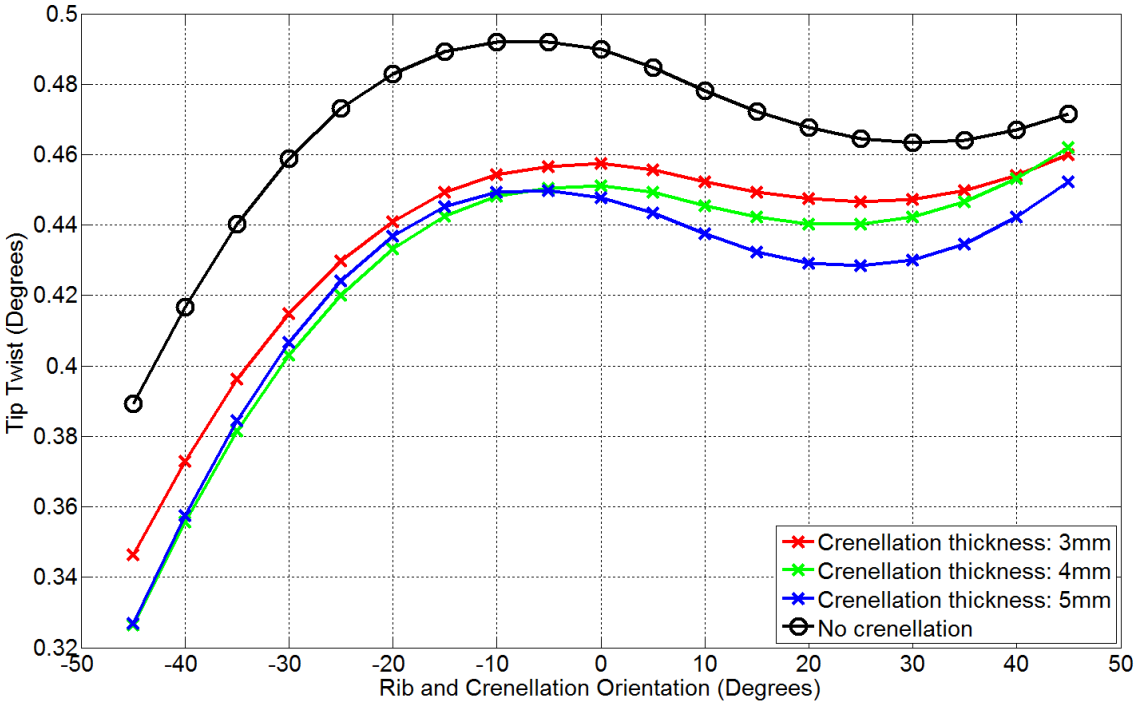

Figure 19. Tip twist for different crenellations thickness and rib/crenellation orientation on a rectangular wing box at an angle of attack of 5° and airspeed of 35m/s.

DISTRIBUTION A. Approved for public release: distribution unlimited.

4.5 Aeroelastic Instability Speed

Figure 20 and Figure 21 show the first aeroelastic instability speed for a rectangular wing box model with different rib/crenellation orientations and different crenellation widths and thicknesses. All wings are subject to the same first two aeroelastic instabilities: (1) a flutter instability with a coalescence of the first bending mode (dominant), second bending mode and the first torsion mode; and (2) a first bending mode divergence instability. The first aeroelastic instability is due to flutter in all cases however wings with rib/crenellation at +45° with crenellation width of 18.52, 11.11, 7.94 and 6.17mm and with crenellation thickness of 4 and 5mm have a divergence instability occurring at almost the same speed (within 0.5-1.6%). Hence, the first aeroelastic instability speed is referred to as the flutter/divergence speed.

The variation of the rib/crenellation orientation has a clear impact on the flutter/divergence speed. The variation of the rib/crenellation orientation from the -5° orientation increases the flutter/divergence speed by up to 7.8%. The lowest and highest flutter/divergence speed for a wing with crenellation's width of 6.17mm is 123.0m/s and 132.6m/s for wings with rib orientation of -5° and -45° respectively. The lack of symmetry by the 0° orientation can be related to the lack of symmetry in the tip displacement and twist curve under aerodynamic loading as explained in Section 4.4.

As mentioned previously, all wings undergo a flutter instability first with five wings having a divergence speed similar to their flutter speed. Nonetheless all wings have the two instability types. The reason for which instability occurs first is impacted by the rib/crenellation orientation. The flutter instability speed is increased by the variation in the rib/crenellation orientation by: (1) primarily increasing the natural frequencies of the first torsional mode and a reduction in natural frequencies of the first two bending modes as shown in Section 4.3 which increase the separation between the modes contributing to flutter and (2) changing the bend-twist coupling of the wing. However, the divergence instability speed is only impacted by the change in bend-twist coupling. Thus, the rib/crenellation orientation leading to an increase in positive tip twist and lift force under aerodynamic loading lowers the divergence instability speed while the flutter instability speed is still increased. At a rib/crenellation orientation of 45° the flutter and divergence instability order can be similar. This is illustrated by Figure 22 which shows the variation of the flutter instability speed and the divergence instability speed with different rib/crenellation orientations for a wing with crenellation width of 11.11mm.

The addition of crenellation at any rib/crenellation orientation increases the flutter/divergence speed when compared to wings with no crenellation of similar rib orientation. For example, at a rib/crenellation orientation of 0° adding crenellation increases the flutter/divergence speed by at least 3.8%. It should be noted that such a wing does not display any bend-twist coupling hence the increase in first aeroelastic instability speed was due to an increase in mode separation as explained in Section 4.3. However when the rib/crenellation orientation is different than 0°, the increase in flutter/divergence speed is also due to a change in wing bend-twist coupling and natural frequencies.

The increase in crenellation width has overall a very small effect on the flutter speed compared to adding crenellation with a maximum increase in flutter/divergence speed of 0.9% compared to the thinnest crenellation considered. Increasing the crenellation thicknesses increases the flutter speed. When varying the crenellation orientation from 3mm to 5mm the flutter speed was found to increase by at least 1.8% in every rib/crenellation orientation considered. This is, once again, primarily due to the increase in mode natural frequency separation.

DISTRIBUTION A. Approved for public release: distribution unlimited.

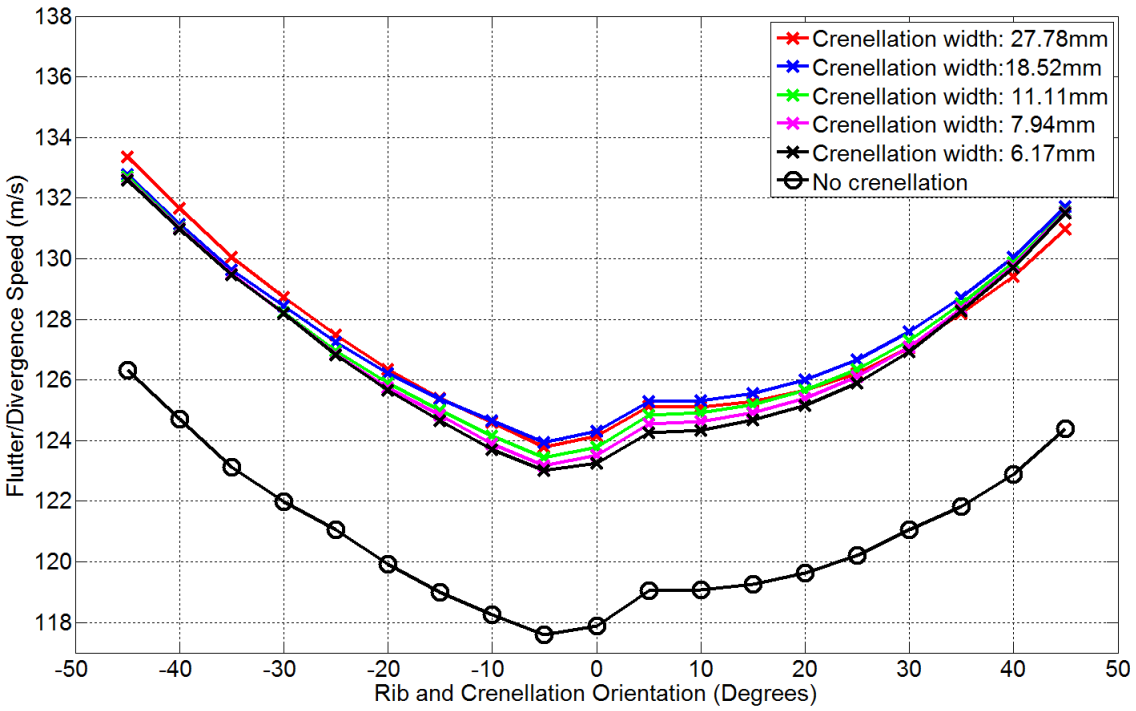

Figure 20. First aeroelastic instability speed for different crenellations width and rib/crenellation orientation on a rectangular wing box.

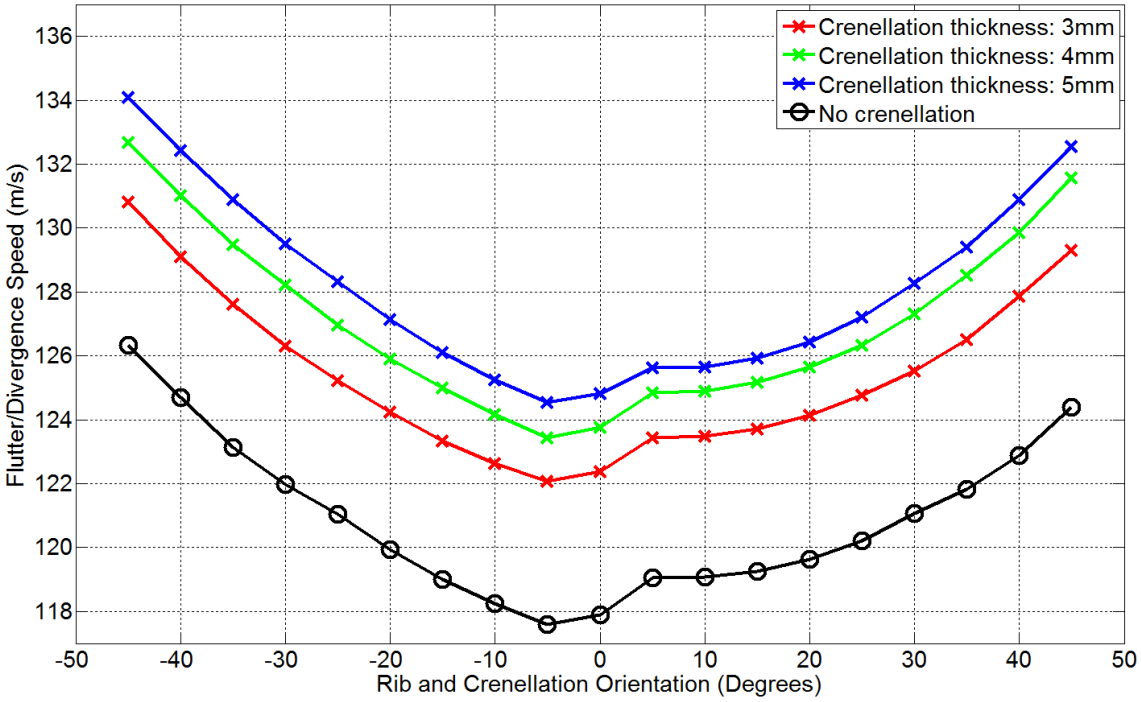

Figure 21. First aeroelastic instability speed for different crenellations thickness and rib/crenellation orientation on a rectangular wing box.

DISTRIBUTION A. Approved for public release: distribution unlimited.

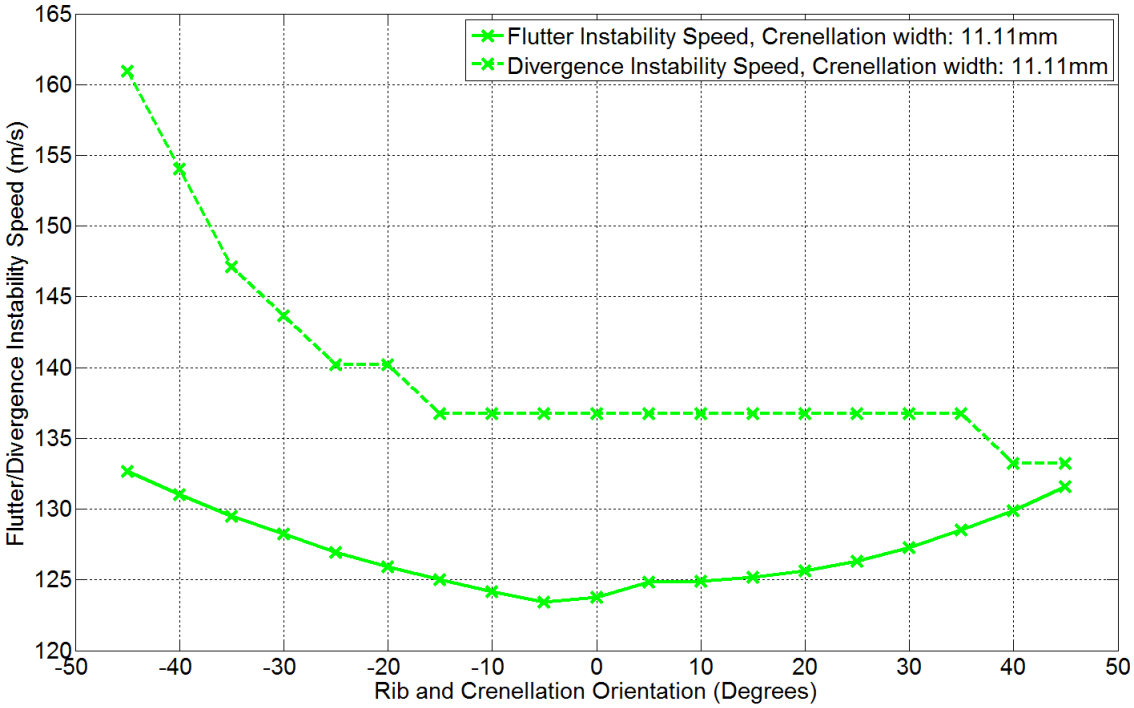

Figure 22. Variation of the flutter instability speed and the divergence instability speed for different rib/Crenellation orientation on a rectangular wing box.

4.6 Bending Moment during Gusts Encounter

Figure 23 and Figure 24 show the maximum root bending moment encounter by a rectangular wing box model during a gust event with different rib/crenellation orientations and different crenellation widths and thicknesses. Varying the rib and crenellation orientation has a large impact on the maximum root bending moment encountered during a gust event. The variation of the rib/crenellation orientation, can reduce the root bending moment by up to 1.7% when compared to the stream wise design. This effect can be explained by the reduction in the tip twist values under a static aerodynamic loading as shown by Figure 17 and Figure 19. It should be noted that the root bending moment versus rib/crenellation orientation curves presented in Figure 23 and Figure 24 have similar overall shapes than the tip twist versus rib/crenellation orientation curves presented in Figure 17 and Figure 19.

At a given rib/crenellation orientation, the addition of crenellations increases the maximum root bending moment during gusts encounter by at least 0.4%, except for wings with crenellations thickness of 3mm with rib/crenellation orientation between [-45°, 0°]. The variation of the crenellation width has a small impact on the root bending moment encounter by the wings. However, Figure 24 show that reducing the thickness of the crenellations reduces the root bending moment. A variation of the crenellation thickness from 5mm to 3mm reduces the root bending moment by up to 1.5%.

It should be noted that although the variation in root bending moment with the rib/crenellation orientation is due to a variation in tip twist, the variation in root bending moment due the addition of crenellations and the variation of the crenellations widths and thicknesses at a given crenellation orientation is primarily impacted by the variation of the natural frequencies and the variation in wing mass. For example, in Figure 24 the highest root bending moment value at any rib/crenellation orientation for wings with crenellations is experienced by the wings with the thickest crenellations. Interestingly this wing design has the lowest first and second bending mode natural frequencies from the other wing designs with crenellations. Its natural frequencies are the furthest away to the natural frequencies of wings without crenellations. Additionally this crenellation width was found to introduce the highest increase in mass.

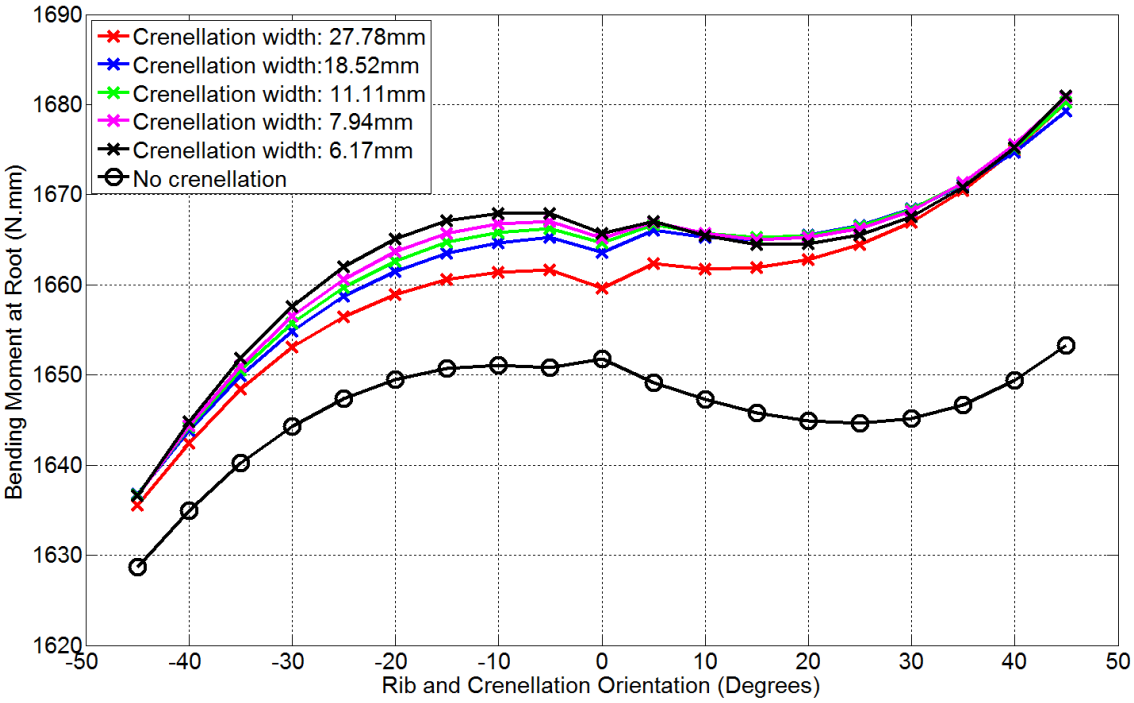

Figure 23. Maximum bending moment at wing root for different crenellations width and rib/crenellation orientation on a rectangular wing box during a gust encounter at an airspeed of 35m/s.

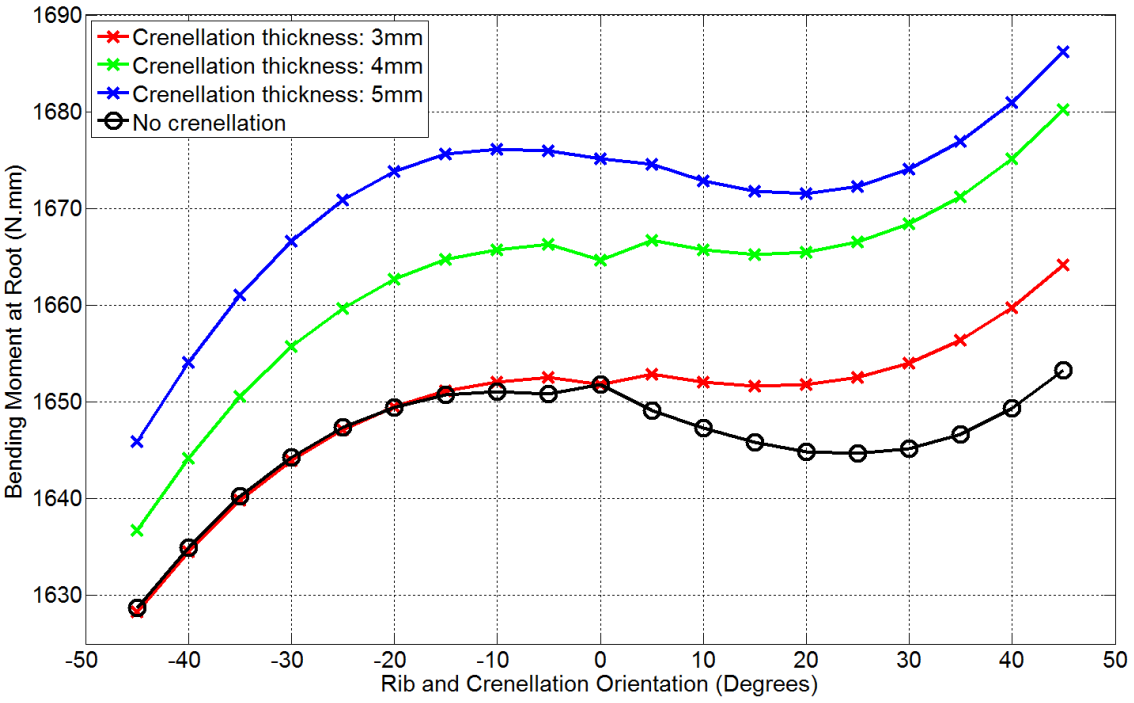

Figure 24. Maximum bending moment at wing root for different crenellations thickness and rib/crenellation orientation on a rectangular wing box during a gust encounter at an airspeed of 35m/s..

DISTRIBUTION A. Approved for public release: distribution unlimited.

5 Material Testing

5.1 Standard Material Test

The material properties of cured Selective Laser Sintering (SLS) polyamide and stereolithography (SLA) resin are reported in Table 2 as specified by the wing manufacturer. So as to validate the Young's modulus value a tensile test was performed with a dog bone specimen (type V) according to ASTM D638-10. The test was carried out using an Instron 3343 electromechanical single column test machine fitted with an Instron 1kN S-beam static load cell with an accuracy of 0.5% of the indicated load. An Imetrum video gauge system [31] was used to measure strain of the specimen with an accuracy of 0.01mm. The results of the tensile test are shown in Figure 25, Figure 26 and Table 3.

Table 2 Cured polyamide and SLA resin material properties as specified by manufacturer.

	Cured SLS polyamide	Cured SLA resin
Young's Modulus (N/mm^2)	1,650.0	2,310.0
Flexural Modulus (N/mm^2)	1,500.0	2,130.0
υ	0.4	N/A
ρ (kg/m^3)	1,150.0	N/A

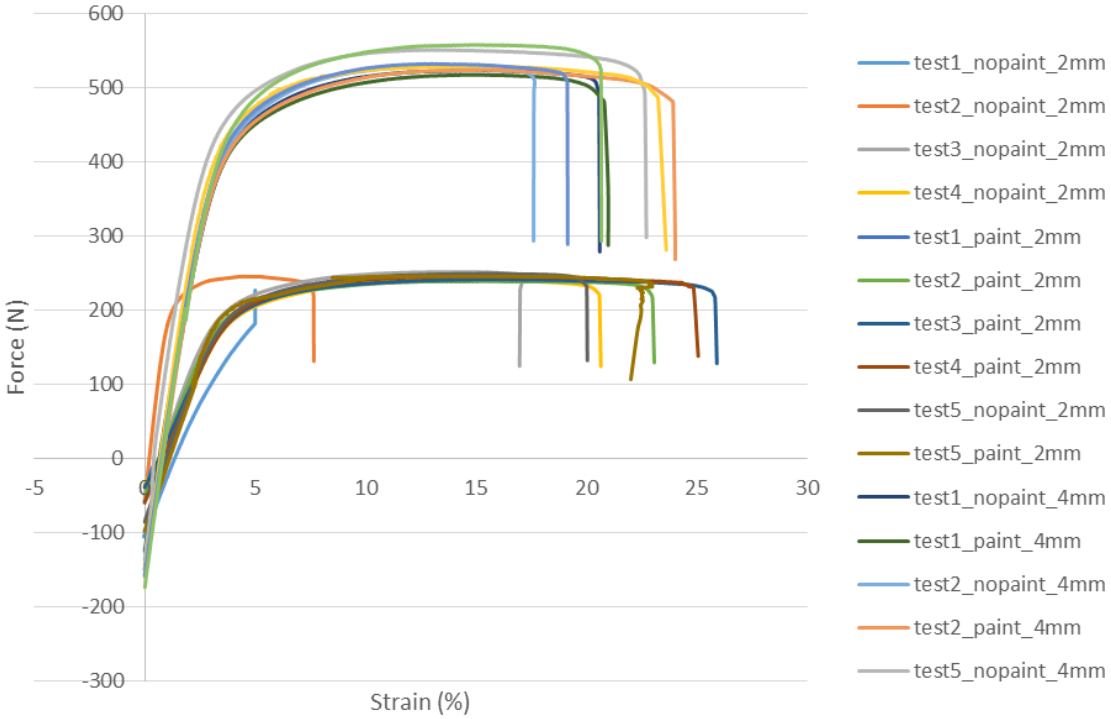

Figure 25. Cured SLS Polyamide Tensile test force vs strain for 2mm and 4mm thickness specimen.

DISTRIBUTION A. Approved for public release: distribution unlimited.

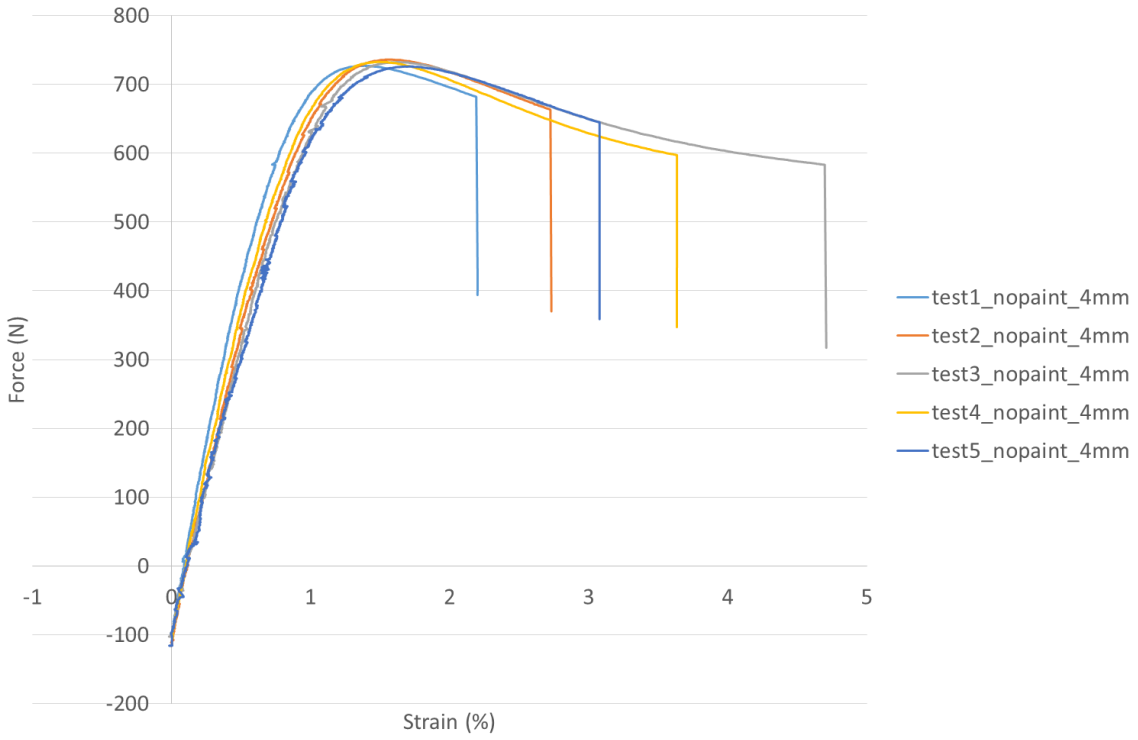

Figure 26. Cured SLA Resin Tensile test force vs strain for 2mm and 4mm thickness specimen.

Table 3 Average Young's modulus values, percentage difference with the manufacturer data and standard deviation for the Cured SLS Polyamide and the SLA resin.

	Cured SLS polyamide				Cured SLA resin
	Painted Specimen	Un-Painted Specimen	2mm Specimen	4mm Specimen	4mm Specimen
Average Young's Modulus (N/mm^2)	1392.5	1386.6	1268.9	1500.3	2413.8
Average % Difference With Manufacturer Data	-15.6	-16.0	-23.1	-9.1	4.5
Standard Deviation (N/mm^2)	156.3	179.0	148.9	96.5	246.4

For the cured SLS polyamide, two different thicknesses were used in this test to assess the impact of component thickness on the material properties. These specimens were also distinguished between painted and non-painted specimens to assess the impact of paint on the wing. The results show that the paint has little effect on the Young's modulus however the thickness of the specimen does. Thicker specimens have more reliable material properties. To confirm this result, a three-point bend test was performed with specimens of 2mm and 4mm depth according to the ASTM D790-10 standard. Force-displacements curves for this test are presented in Figure 27 and flexural modulus data are presented in Table 4. These values confirm this finding as the 4mm specimen curves show less scatter than the 2mm specimen curves.

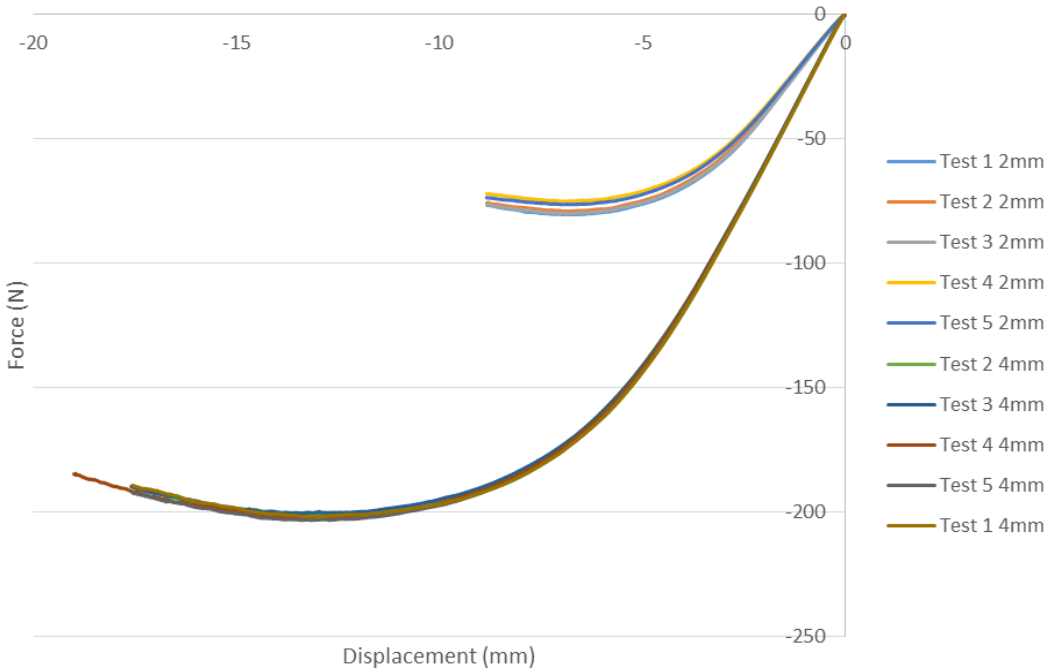

Figure 27. 3 point bend test force vs displacement for 2mm and 4mm thickness specimen.

Table 4 Average flexural modulus values, percentage difference with the manufacturer data and standard deviation.

	2mm Specimen	4mm Specimen
Average Flexural Modulus (N/mm^2)	1433.0	1795.6
Average % Difference With Manufacturing Data	-4.5	19.7
Standard Deviation (N/mm^2)	50.7	25.6

Based on the experience gathered from the cured SLS polyamide testing, the tensile test was performed for 4mm thick, un-painted specimen. The results show acceptable level of variation in tensile modulus with the manufacturer's data.

Finally, a stress relaxation test was carried out for both materials. The test consists in maintaining a constant displacement of 1mm on a 4mm specimen over time. Load reduction over time is shown in Figure 28 and clearly highlights that both polymers undergoes some stress relaxation. The cured SLA resin is subject to more stress relaxation than the cured SLS polyamide.

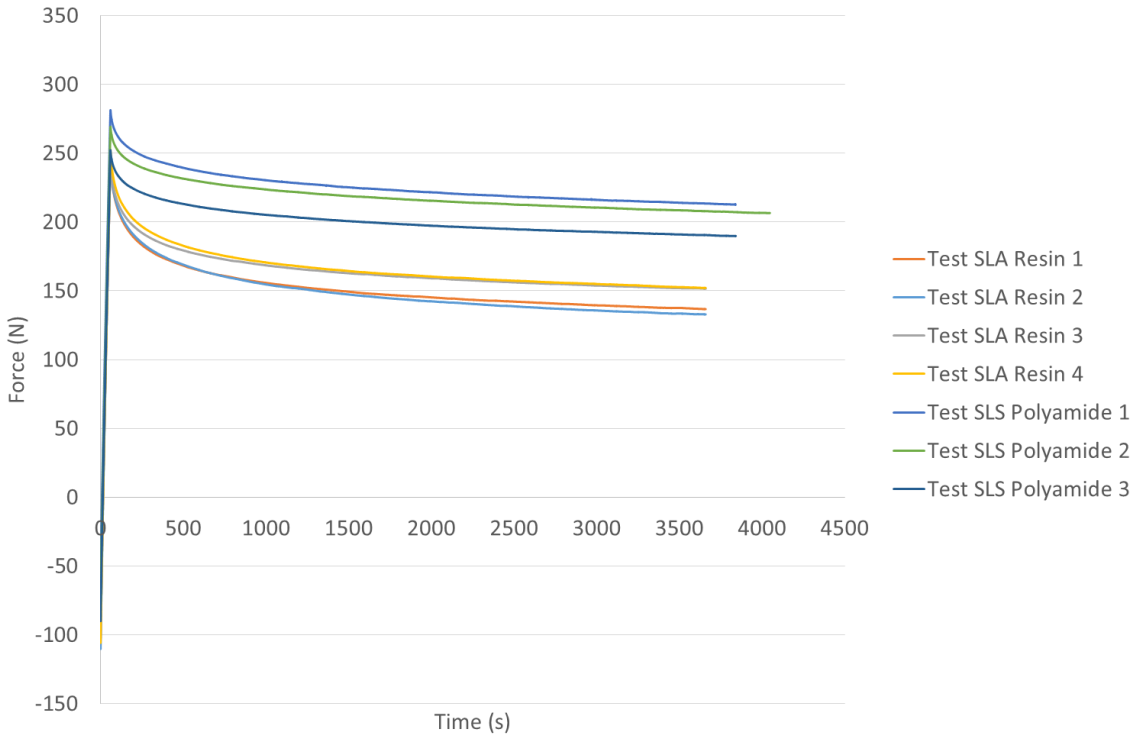

Figure 28. Force versus time illustrating stress relaxation when specimen are hold at a displacement of 1mm for both cured SLS polyamide and SLA resin specimen.

5.2 Impact of Print Direction on Material properties

5.2.1 Variation in Flexural Modulus

Both materials considered are manufactured by selective solidification of material. The part is resting on a piston which moves in the Z direction of the printer. Thus the machines solidify layers in the X-Y plane. The possibility of material anisotropy resulting from the laser sintering manufacturing process was investigated using three point bend test. A series of three point bend test specimen were manufactured in two planes of the machine: X-Y and X-Z plane. The test specimens were manufactured as one part where every test specimen is attached to at least one another hence forcing the machine to print the specimen in one of the three dimensional axis. Additionally, some specimen were oriented at an angle. A picture of the manufactured part is shown in Figure 29 and a CAD drawing of the part in the machine bath is shown in Figure 30.. The three point bend test specimen were tested according to ASTM D790-10 standard. Displacement measurement was performed using the video gauge system. Both the cured SLS polyamide and the cured SLA resin were tested.

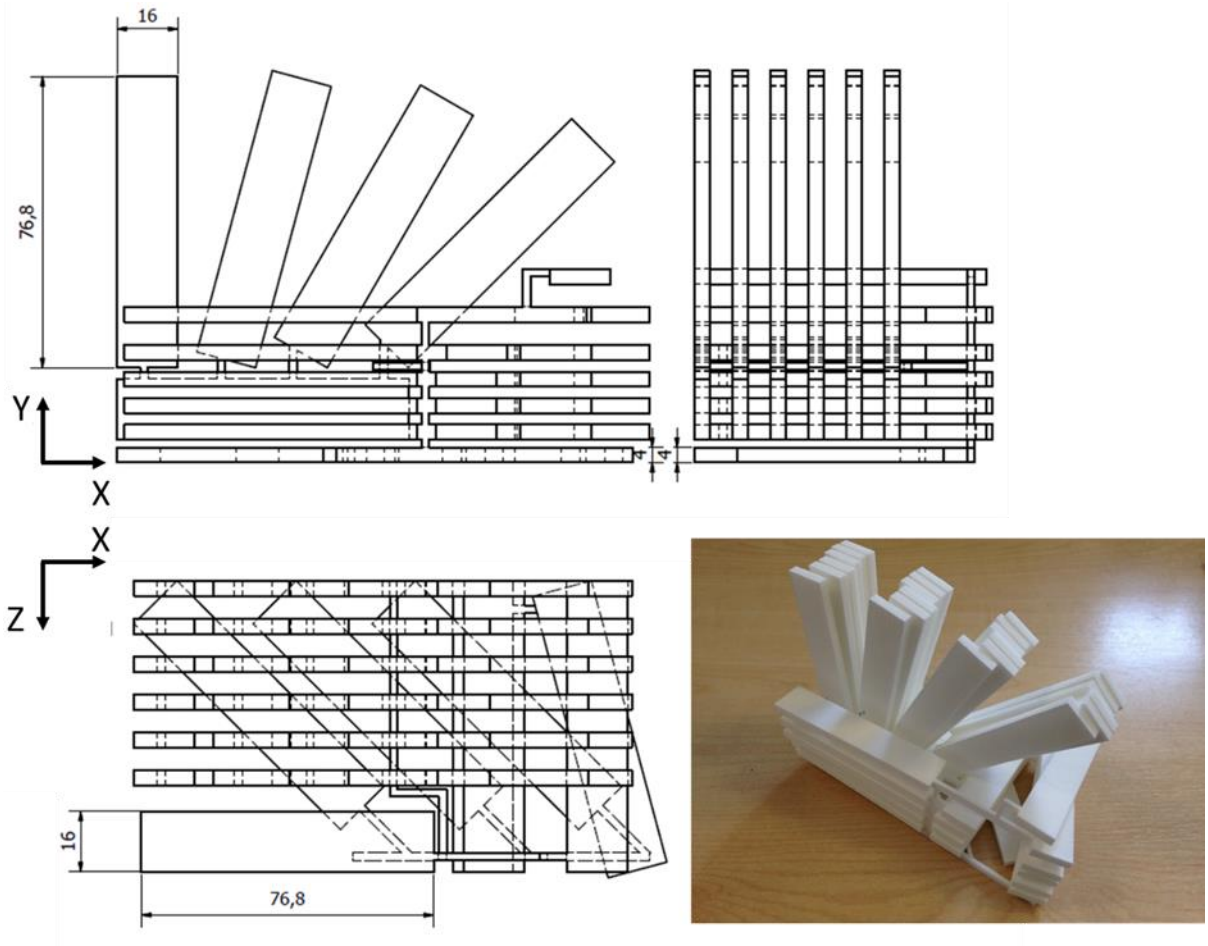

Figure 29. Three Dimensional Three Point Bend Test Specimen.

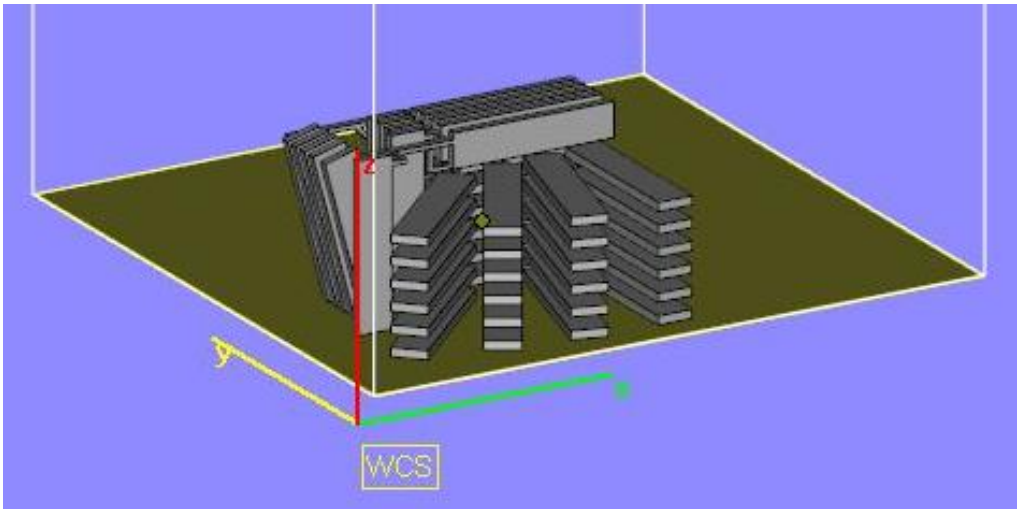

Figure 30. Three Dimensional Three Point Bend Test Specimen in the Printer Bath where Z is the direction in which the piston holding the part is moving.

Average flexural modulus and percentage difference with the manufacturer data for the three point bend specimen printed in different directions is presented in Table 5 and Table 6 for the cured SLS polyamide and cured SLA resin specimen respectively. Figure 31 and Figure 32 show the variation of the average flexural modulus with a change in specimen orientation for the cured SLS polyamide and

cured SLA resin specimen respectively. The specimen direction is specified by the angle in degrees between the length of the specimen and an axis in of the two planes the X-Y or X-Z plane of the printer.

When considering cured SLS polyamide specimen the direction at which the specimen are printed has a large impact on the flexural modulus as specimen printed in the X-Z plane of the machine have much lower flexural modulus than the one printed in the X-Y plane (-21% and -6% respectively compared to manufacturer data). This can be explained by the positioning of layer interphases in the length and/or width of the specimen. This is further confirmed by the fact that during testing specimen printed in the 0^o, Z and 15^o, Z direction were found to break while all other specimen were only plastically deformed.

It should be noted that printing the specimen at an angle also has an impact on the flexural properties. In the X-Z plane, the rotation of the specimen from 0^o to the Z-axis to 90^o to the Z-axis creates an increase in flexural modulus. Once again this can be related to the position of the layer interfaces: at (0^o, Z) the layer interfaces run parallel to the specimen's width while at (90^o,Z) they run parallel to the specimen's length.

When considering cured SLA resin specimen the flexural modulus does not vary significantly with the direction of the specimen in the printer. No significant change in failure mechanism was recorded during testing of the specimen.

Table 5. Cured SLS polyamide average flexural modulus values and percentage difference with the manufacturer data for the 3 point bend specimen printed in different directions.

Specimen Orientation	0^o, Z	15^o, Z	45^o, Z	90^o, Z	0^o, Y	15^o, Y	30^o, Y	45^o, Y	90^o, Y
Average Flexural Modulus (N/mm^2)	1129.3	1151.1	1204.0	1239.0	1534.1	1282.0	1307.9	1459.4	1457.9
Average % Difference With Manufacturing Data	-24.7	-23.3	-19.7	-17.4	2.3	-14.5	-12.8	-2.7	-2.8

Table 6. Cured SLA resin average flexural modulus values and percentage difference with the manufacturer data for the 3 point bend specimen printed in different directions.

Specimen Orientation	0^o, Z	15^o, Z	45^o, Z	90^o, Z	0^o, Y	15^o, Y	30^o, Y	45^o, Y	90^o, Y
Average Flexural Modulus (N/mm^2)	2660.4	2584.1	2627.2	2745.8	2614.3	2602.4	2588.1	2593.4	2445.4
Average % Difference With Manufacturing Data	24.9	21.3	23.3	28.9	22.7	22.2	21.5	21.8	14.8

DISTRIBUTION A. Approved for public release: distribution unlimited.

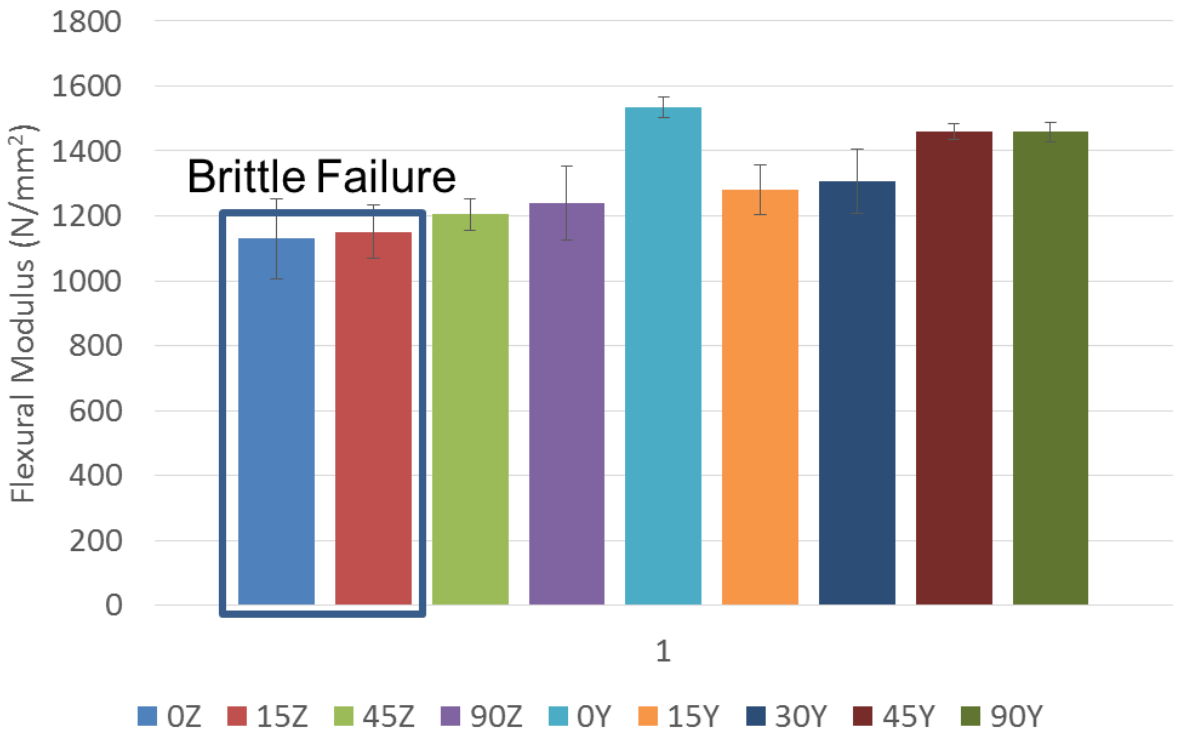

Figure 31. Cured SLS polyamide Average Flexural Modulus for three point bend specimen printed in different directions in the printer.

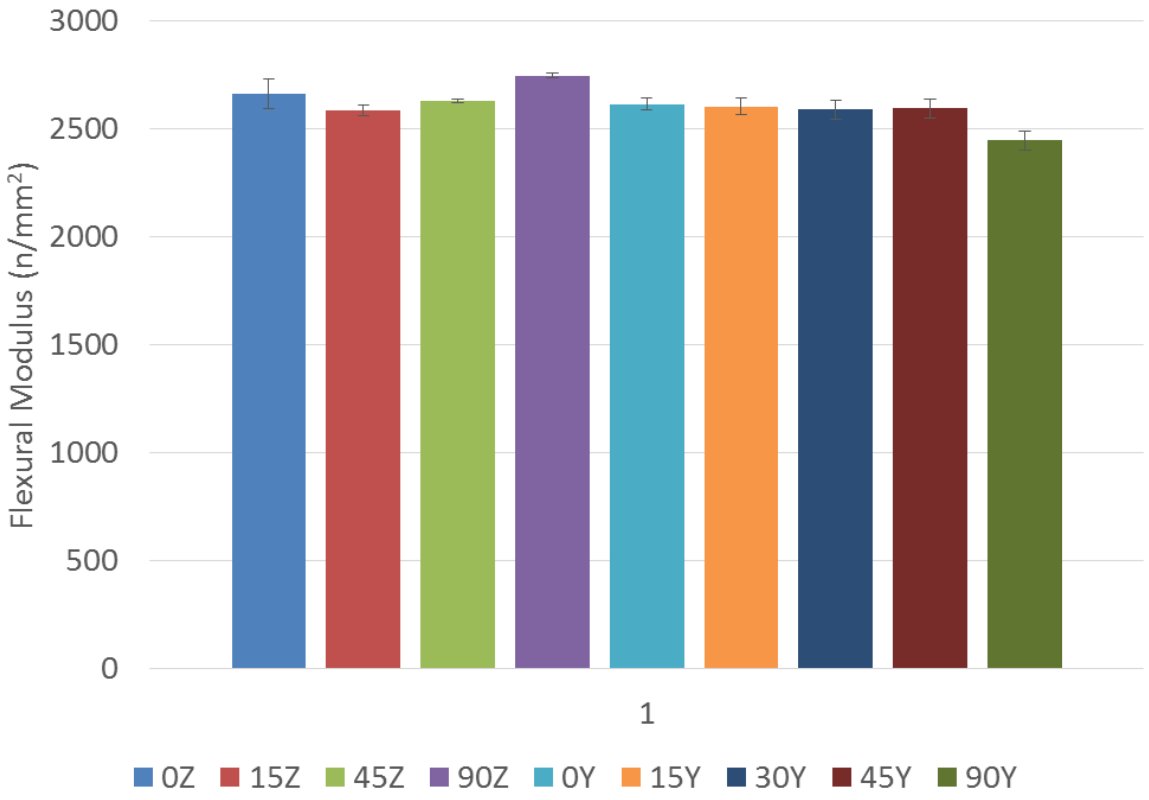

Figure 32. Cured SLA Resin Average Flexural Modulus for three point bend specimen printed in different directions in the printer.

DISTRIBUTION A. Approved for public release: distribution unlimited.

To illustrate the effect of the printing direction on both materials, Figure 33 shows the variation in flexural modulus between specimens printed with their length in the X-Y or X-Z planes. The flexural modulus of the cured SLS polyamide and cured SLA resin specimen vary between the two planes on average by 19.3% and -3.2%. Clearly, the flexural modulus of the cured SLS polyamide specimen is dependent of the direction at which the specimen is placed in the printer which is not the case for cured SLA resin specimen.

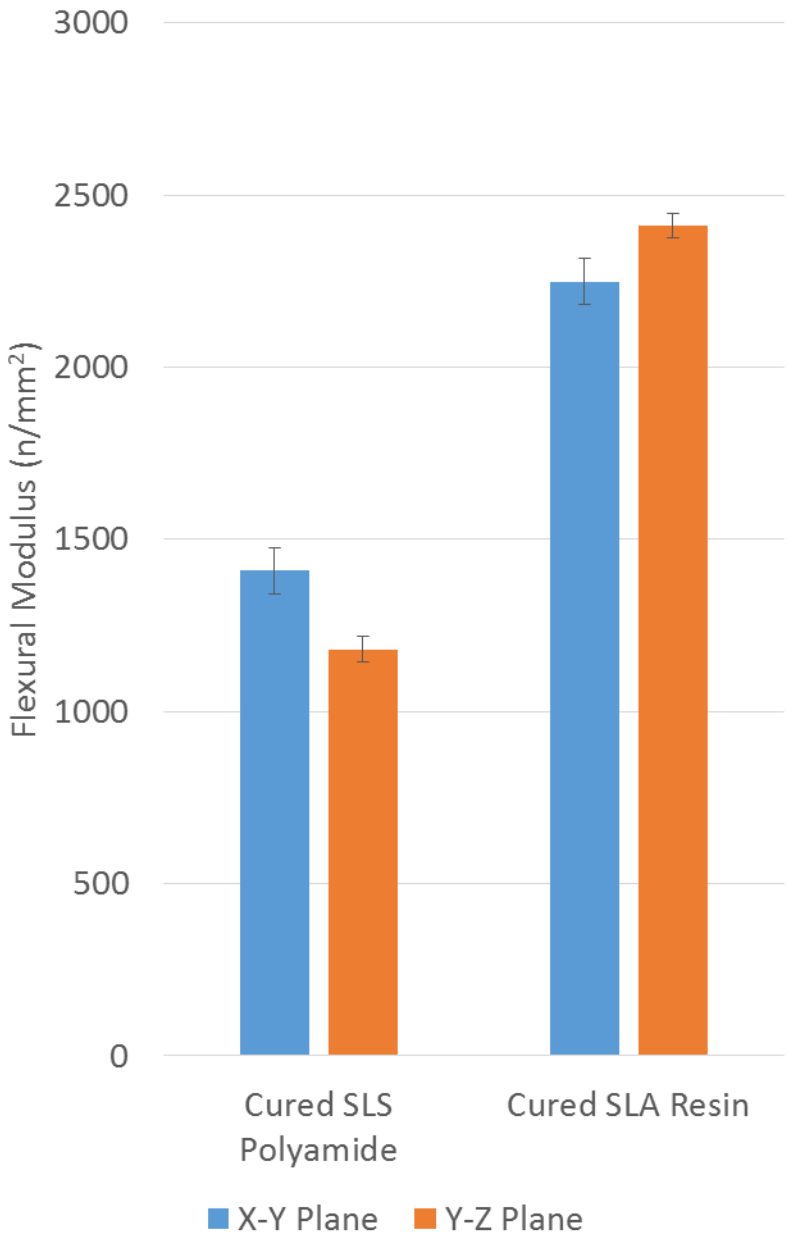

Figure 33. Cured SLS polyamide and cured SLA resin average Flexural Modulus of the specimen placed in the X-Y and Y-Z planes.

5.2.2 SEM Investigation

In order to understand the variation in flexural modulus shown in cured SLS polyamide specimen, the different three point bend test specimen along with a sample of the SLS polyamide powder were

analysed using a Scanning Electron Microscope (SEM). Figure 34 shows representative SEM images for both a cured SLS polyamide specimen and uncured polyamide powder. Comparing the powder SEM image with the cured specimen solidification features are clearly visible but no layered solidification features can be distinguished. SEM images for the different sides of the cured specimen were taken and similar conclusion were reached.

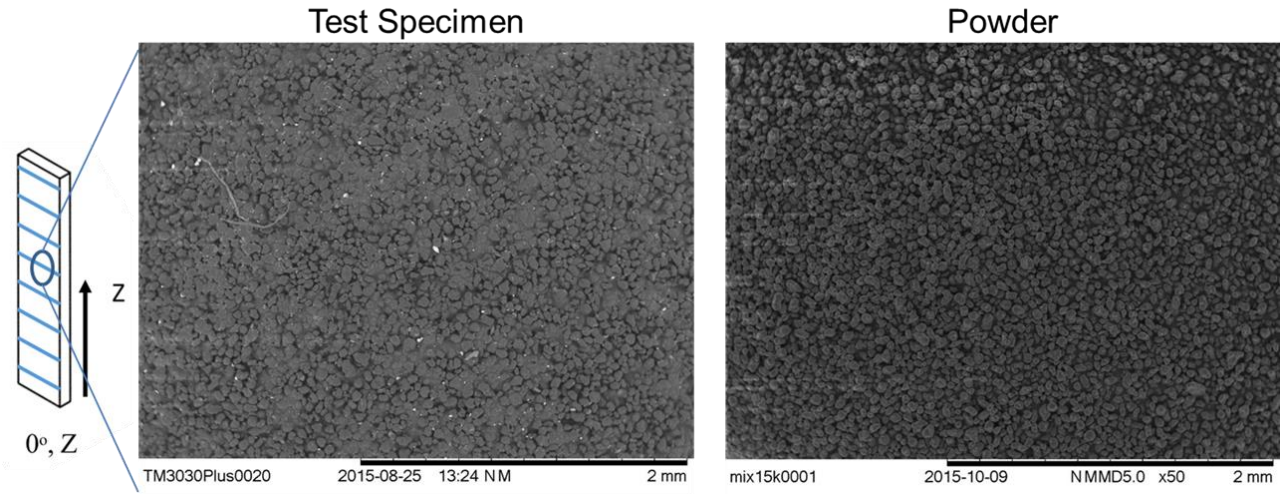

Figure 34. SEM Image of a Three-Point Bend Specimen.

5.2.3 **Microtomography Investigation**

To further investigate the material anisotropy in the cured SLS polyamide specimen, microtomography imagining on three specimen printed in different directions (0^o, Z; 0^o, Y; 90^o, Y) was performed. VG StudioMax holes/defects analysis tool was used to analyze the location of voids and defects in the specimen. Preliminary analysis revealed a material with many voids as shown by Figure 35. These voids were found to be predominantly perpendicular with the z-direction of the printer. Further analysis is on-going to confirm these results.

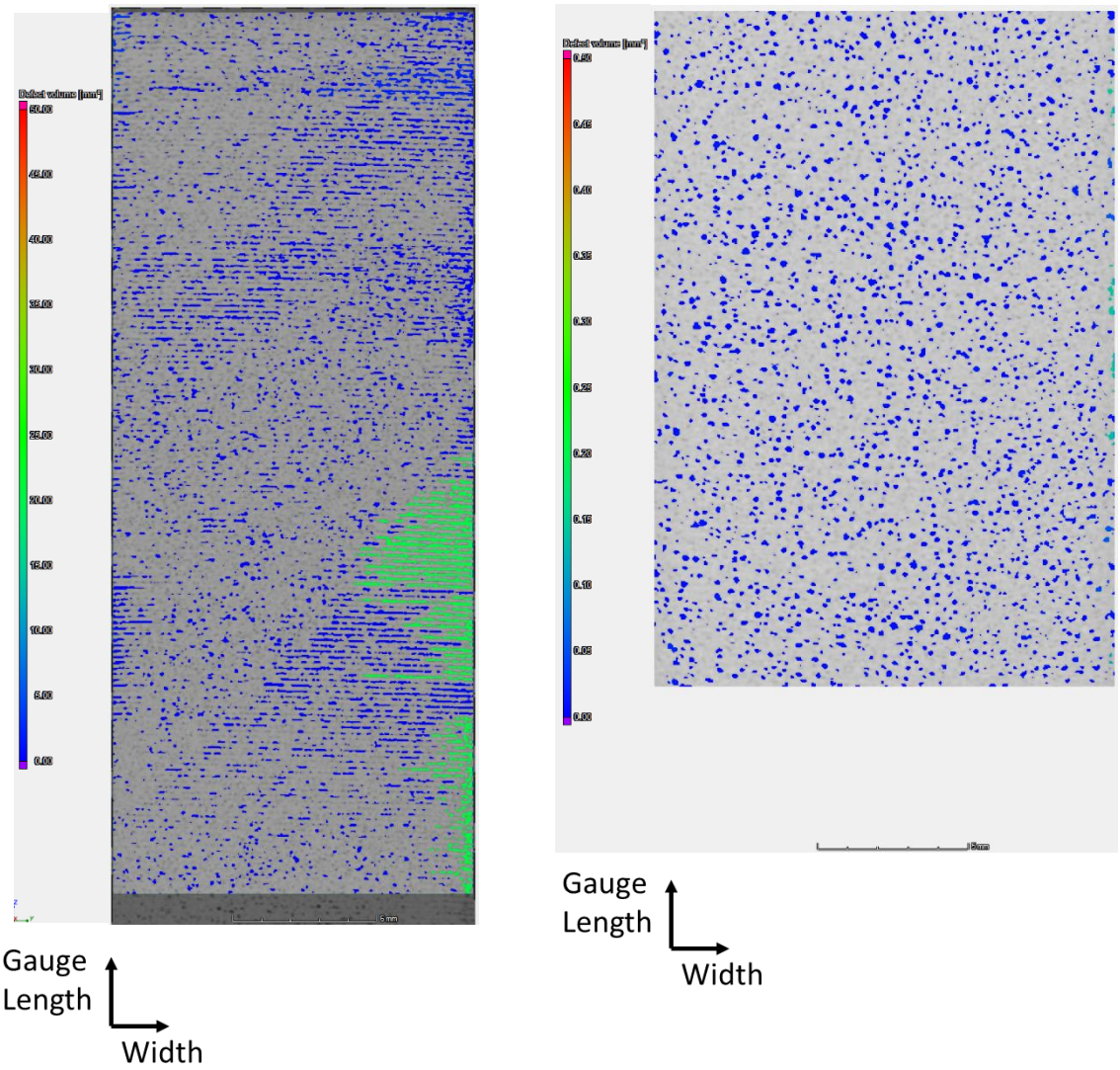

(a) Specimen 0°, Z. (b) Specimen 0°, Y

Figure 35. Microtomography images of two three point bend specimen oriented in different directions in the printer. The colour represent the volume of defects found by VG Studio Max holes/defects detection tool.

5.3 Conclusions on material testing

A cured SLS polyamide and a cured SLA resin materials were tested. Experiments to characterise the Young's modulus, flexural modulus and stress relaxation were performed. The cured SLA resin material had higher Young's and flexural moduli than the cured SLS polyamide material and was subject to more stress relaxation than the cured SLS polyamide material.

An investigation of the flexural modulus variation with the orientation of the specimen in the printer revealed that specimen printed in the cured SLS polyamide material can have flexural modulus value vary by up to 19.3% with the orientation of the specimen in the printer. In the case of the cured SLA resin material, only a 3.2% variation was recorded. Microtomography of the cured SLS polyamide specimen revealed large regions of voids. These voids regions were predominantly perpendicular with the z-direction of the printer (direction of motion of the piston).

Although the cured SLA resin material did not display as much material anisotropy as the cured SLS polyamide, the cured SLA resin material had a few major drawbacks. First, the SLA resin material showed higher stress relaxation than the SLS polyamide. Secondly, the material had rate dependent material response: brittle failures were observed when the material was impacted at high rate but slow

test such as the test presented in this section lead to plastic deformation of the specimen. Finally, the cured SLA resin was twice as expensive as the cured SLS polyamide material. Thus the wings were manufactured in SLS polyamide material.

6 Wing Manufacturing and Manufacturing Quality Control

6.1 Wing Manufacturing

It was decided to manufacture wings using the SLS polyamide printing process. Throughout this project several orders have been made with wings with and without crenellations and with different rib/crenellation orientations and with 4mm thick spar and ribs and 2mm thick skin. The different designs ordered are shown in Table 7. In addition, the direction at which the parts were placed in the printer is specified. The three possible directions are shown on

Figure ***36***.

When considering crenellations, only one crenellation width of 11.11m was considered. It should be noted that the wings with rib/crenellation stream wise are labelled: Baseline with Crenellations and Baseline with Alternate Crenellations. The Baseline with Crenellations design has the first crenellation after the root half-rib. Hence every rib bay had two (or three) regions of standard skin thickness of 2mm and three (or two) crenellations with a skin thickness of 4mm as shown Figure 4. The exact number for a particular rib bay was dependent on the location of the rib e.g. the first rib bay has two regions of standard skin thickness and three crenellations while the second rib bay has three regions of standard skin thickness and two crenellations. A manufacturing error meant that the Baseline with Alternate Crenellations design had a total of 22 crenellations as the region after the root was of standard thickness. Hence every rib bay of that wing had three/two regions of standard skin thickness of 2mm and two/three crenellations with a skin thickness of 4mm as shown Figure 2 (e.g. the first rib bay has three regions of standard skin thickness and two crenellations while the second rib bay has two regions of standard skin thickness and three crenellations).

A rectangular root section was manufactured with each wing, as shown in

Figure ***37***, to permit the fixation of the wings to the bench/wind tunnel. Four small holes were placed in the ribs to remove excess powder trapped after manufacturing. A small amount of powder remained trapped in the wings as can be seen by the dark areas on

Figure ***37***. Finally, two coats of white paint were applied on both sides and black paint speckles were applied on one side of the wings as shown by

Figure ***37*** to enable the use of Digital Image Correlation (DIC). The variation in wing mass with and without paint is shown in Table 7.

DISTRIBUTION A. Approved for public release: distribution unlimited.

Table 7. Details of the different orders placed to the supplier with ordered wing designs, mass of the wings before and after being painted and orientation of the wing in the printer. All the wings were made using SLS polyamide material.

Order Number	Wing Design	Mass - No Paint (g)	Mass - With Paint (g)	Orientation of Wing in Printer
1	Baseline	346	352	a
1	Baseline With Crenellations, Alternate	384	390	a
1	Ribs @ 45 Degrees With Crenellations	377	383	a
2	Ribs @ 30 Degrees	350	355	b
2	Ribs @ 40 Degrees	361	369	b
2	Ribs @ 45 Degrees	370	376	b
2	Ribs @ 45 Degrees With Crenellations	417	422	b
3	Baseline With Crenellations, Alternate	390	399	b
3	Baseline	320	327	b
4	Baseline	336	342	c
4	Ribs @ 15 Degrees	350	358	c
4	Ribs @ 30 Degrees	321	330	c
4	Ribs @ 40 Degrees	355	362	c
5	Baseline	321	326	b
5	Ribs @ -30 Degrees	337	338	b
5	Ribs @ -40 Degrees	357	360	b
5	Ribs @ 45 Degrees	346	350	b
5	Ribs @ -45 Degrees	347	356	b
5	Baseline With Crenellations	379	381	b
5	Ribs @ -30 Degrees With Crenellations	372	375	b
5	Ribs @ -40 Degrees With Crenellations	384	387	b
5	Ribs @ -45 Degrees With Crenellations	394	401	b
5	Ribs @ 45 Degrees With Crenellations	379	397	b
6	Baseline	351	364	b
6	Ribs @ -30 Degrees	336	350	b
6	Ribs @ -40 Degrees	354	372	b
6	Ribs @ 45 Degrees	312	330	b
6	Ribs @ -45 Degrees	279	305	b
6	Baseline With Crenellations	395	411	b
6	Ribs @ -30 Degrees With Crenellations	351	368	b
6	Rib @ -40 Degrees With Crenellations	335	358	b
6	Rib @ -45 Degrees With Crenellations	349	369	b
6	Rib @ 45 Degrees With Crenellations	406	423	b

DISTRIBUTION A. Approved for public release: distribution unlimited.

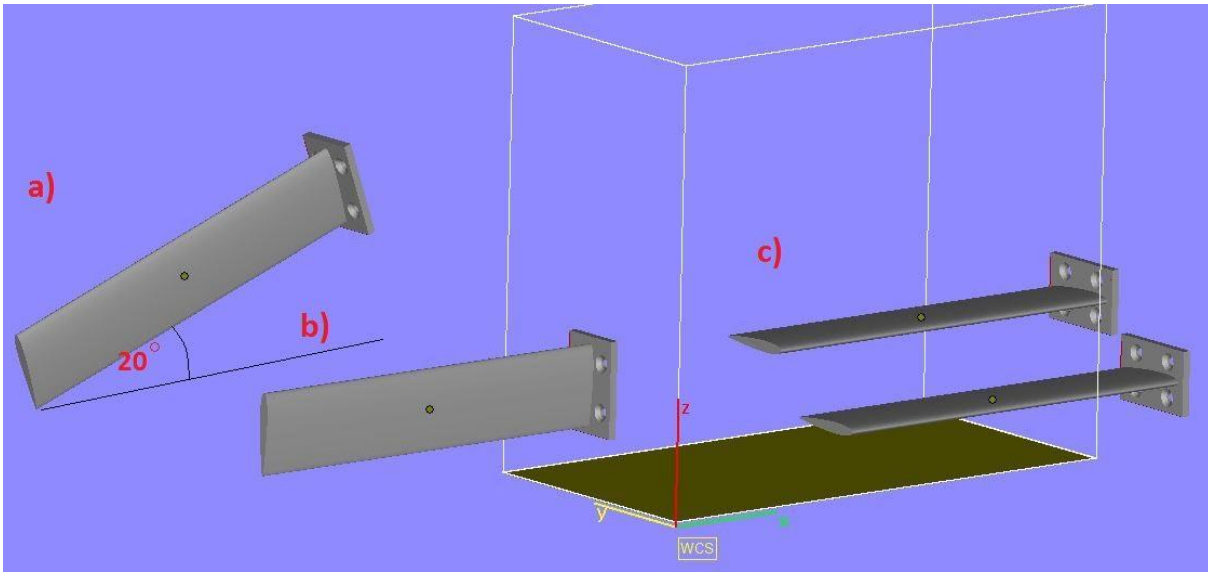

Figure 36. Orientation of Parts in SLS Printer. Printer piston moves in the z direction.

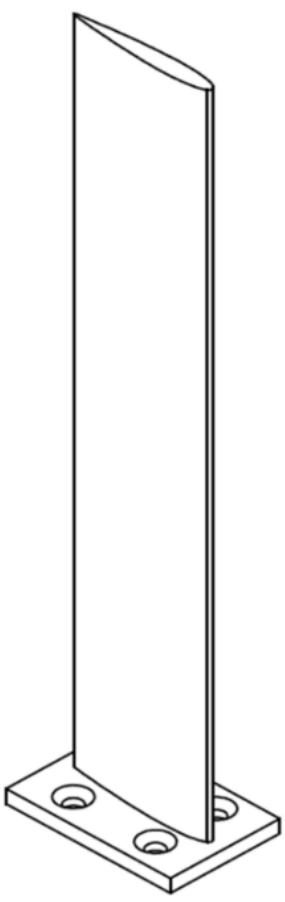

(a) CAD file sent to the manufacturer

(b) View of the excess powder trapped in the wing

(c) Digital image correlation paint pattern on a wing

Figure 37. Illustration of the wing manufacturing process

6.2 Manufacturing Quality Control

A motivation for manufacturing the wings using an additive manufacturing method is for the simplicity such methods offer to produce structure with complex shapes. In the case of a wing this relates to the internal wing structure and the complex external aerofoil profile required for the wind tunnel test. Prior to perform any test there is a need to understand the quality of the manufacturing and its repeatability. Hence, to control the quality of the manufacturing process the quality of skin surface and a series of external and internal dimensions were taken. The mass variation between similar wing designs gives an appreciation for the repeatability of the manufacturing process.

6.2.1 Skin Surface Quality

A visual inspection of the skin surface of the different wings was performed to assess any noticeable differences. Skin surface finish is paramount for wind tunnel testing where any defects such as dents or excessive roughness of the skin would change the aerodynamic performance. The skin surface quality was quantified into three categories: “good”: no visible damage or variations; “fair” slight visible skin variations; and “bad”: unacceptable damages/variations, not suited for wind tunnel tests as shown by Figure 38. Table 8 shows the skin surface quality for the different wings ordered. Overall, a clear dependence was found between the skin surface quality and the orientation of the wing in the printer. Orientation c) leads to the formation of grooves on the skin surface of the wings as shown by Figure 38. Orientation a) gave the best skin surface followed by orientation b).

Figure 38. Illustration of a “bad” skin surface finish.

DISTRIBUTION A. Approved for public release: distribution unlimited.

Table 8. Skin Surface Quality of the Different Wings Ordered.

Order Number	Wing Design	Skin Surface Quality	Orientation of Wing in Printer
1	Baseline	Good	a
1	Baseline With Crenellations, Alternate	Good	a
1	Ribs @ 45 Degrees With Crenellations	Good	a
2	Ribs @ 30 Degrees	Fair	b
2	Ribs @ 40 Degrees	Fair	b
2	Ribs @ 45 Degrees	Fair	b
2	Ribs @ 45 Degrees With Crenellations	Fair	b
3	Baseline With Crenellations, Alternate	Fair	b
3	Baseline	Fair	b
4	Baseline	Bad	c
4	Ribs @ 15 Degrees	Bad	c
4	Ribs @ 30 Degrees	Bad	c
4	Ribs @ 40 Degrees	Bad	c
5	Baseline	Fair	b
5	Ribs @ -30 Degrees	Fair	b
5	Ribs @ -40 Degrees	Fair	b
5	Ribs @ 45 Degrees	Fair	b
5	Ribs @ -45 Degrees	Fair	b
5	Baseline With Crenellations	Fair	b
5	Ribs @ -30 Degrees With Crenellations	Fair	b
5	Ribs @ -40 Degrees With Crenellations	Fair	b
5	Ribs @ -45 Degrees With Crenellations	Fair	b
5	Ribs @ 45 Degrees With Crenellations	Fair	b
6	Baseline	Fair	b
6	Ribs @ -30 Degrees	Fair	b
6	Ribs @ -40 Degrees	Fair	b
6	Ribs @ 45 Degrees	Fair	b
6	Ribs @ -45 Degrees	Fair	b
6	Baseline With Crenellations	Fair	b
6	Ribs @ -30 Degrees With Crenellations	Fair	b
6	Rib @ -40 Degrees With Crenellations	Fair	b
6	Rib @ -45 Degrees With Crenellations	Fair	b
6	Rib @ 45 Degrees With Crenellations	Fair	b

6.2.2 **External Measurements**

External measurements were made using a 3D laser scanner FARO Edge ScanArm [32] with an accuracy of ±0.05mm. 3D laser scanning is a common quality control method which consists in scanning the part produced to create a point cloud measurement representation of the part. From this point cloud, measurement of external dimensions of the wing can be made as well as manufacturing induced deformation such as twist and bending due to warping during curing. The point cloud was

divided into 11 equally spaced sections with section 0 and 10 at the root and tip respectively. For simplicity, the root was defined 1mm from the plane connecting the wing with the rectangular root section. To avoid mesh dependence error the sectional deflection and twist were found by interpolation through the mesh data on the cover of the wing. Wings from order 6 were checked using this method after their arrival from the manufacturer.

Figure 39, Figure 40 and Figure 41 show the sectional bending deflection, sectional twist and forward/aft trailing edge displacement with respect to the root section and trailing edge. Table 9 shows the sectional average chord length, standard deviation and percentage difference with the CAD chord length (102mm) for the different wings of order 6. The variation in sectional chord length for the different wings was acceptable with a maximum difference from the CAD chord length of 0.8mm. Hence the dimension tolerances is considered to be good however some wings displayed clear bending and forward/aft deformation. For example, the wing with ribs and crenellations orientated at-40^{o} had a 9.6mm and 3.8mm bending and forward/aft deformations. These deformations could be due to deformation of the wing during the manufacturing process and/or from deformation during the analysis due to low material properties and/or high internal geometry tolerance. Finally, only small amount of twist deformation was recorded with a maximum twist deformation of 0.5^{o} at the tip for the wing with ribs at -40^{o}.

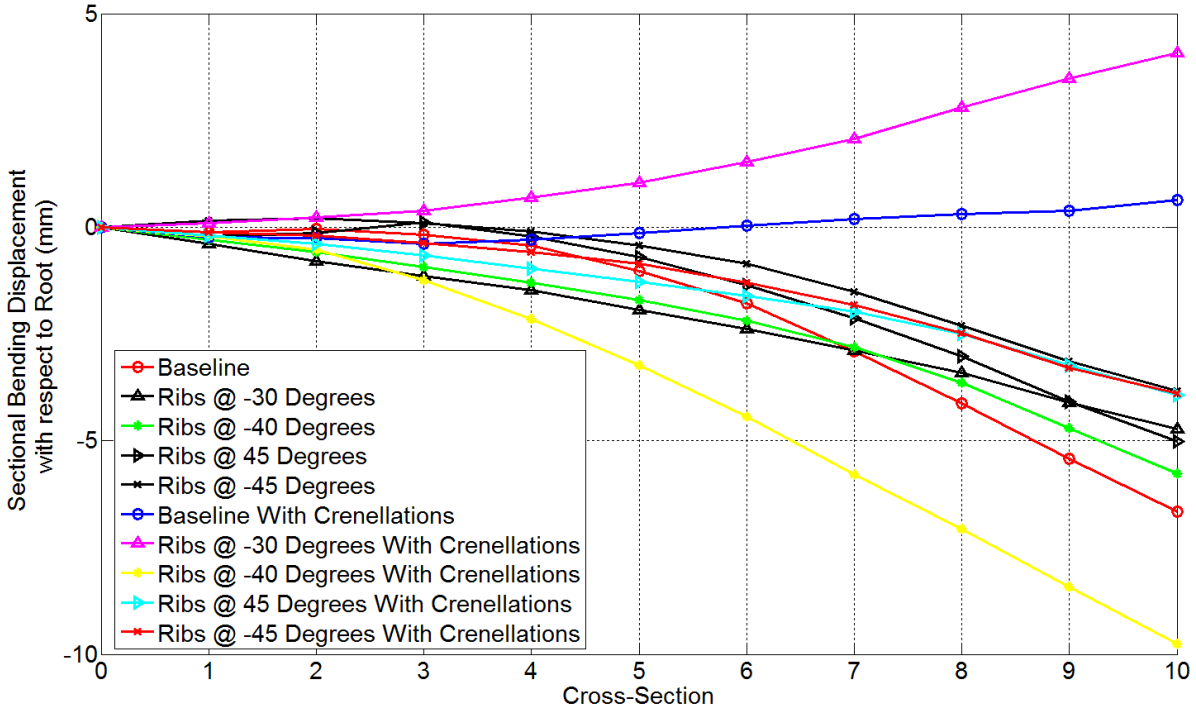

Figure 39. Sectional Displacement with respect to the Wing Root. Section 10 is at the wing tip.

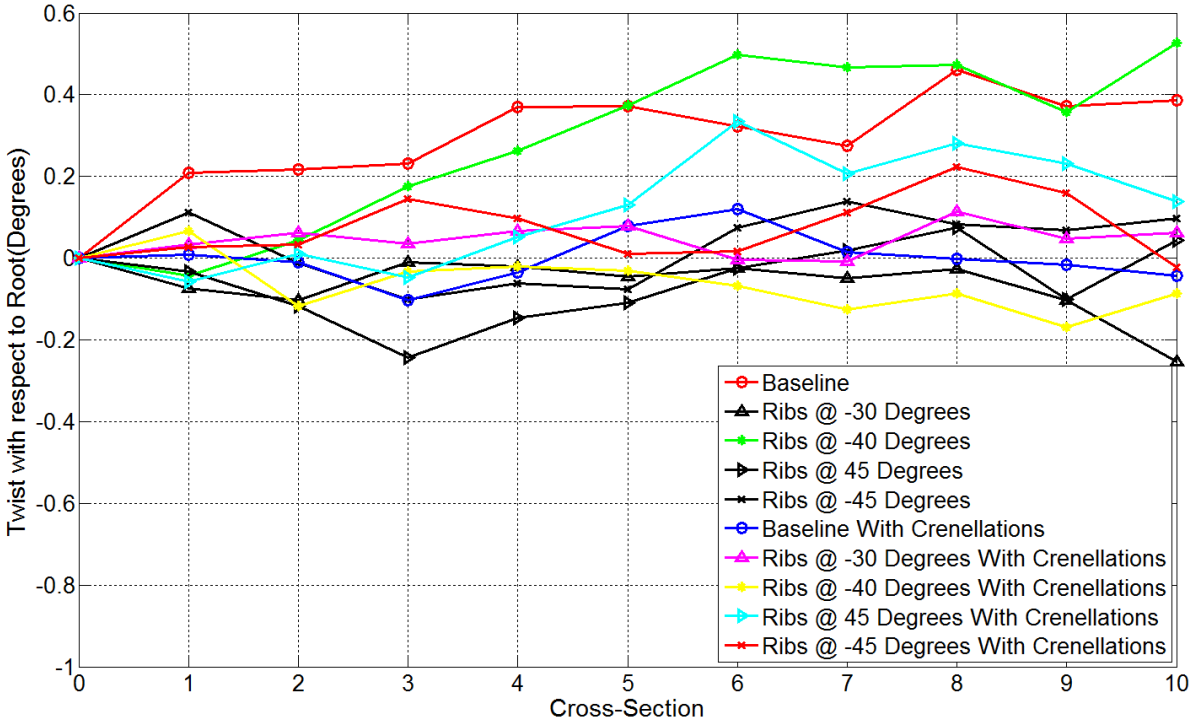

Figure 40. Sectional Twist with respect to the Wing Root. Section 10 is at the wing tip.

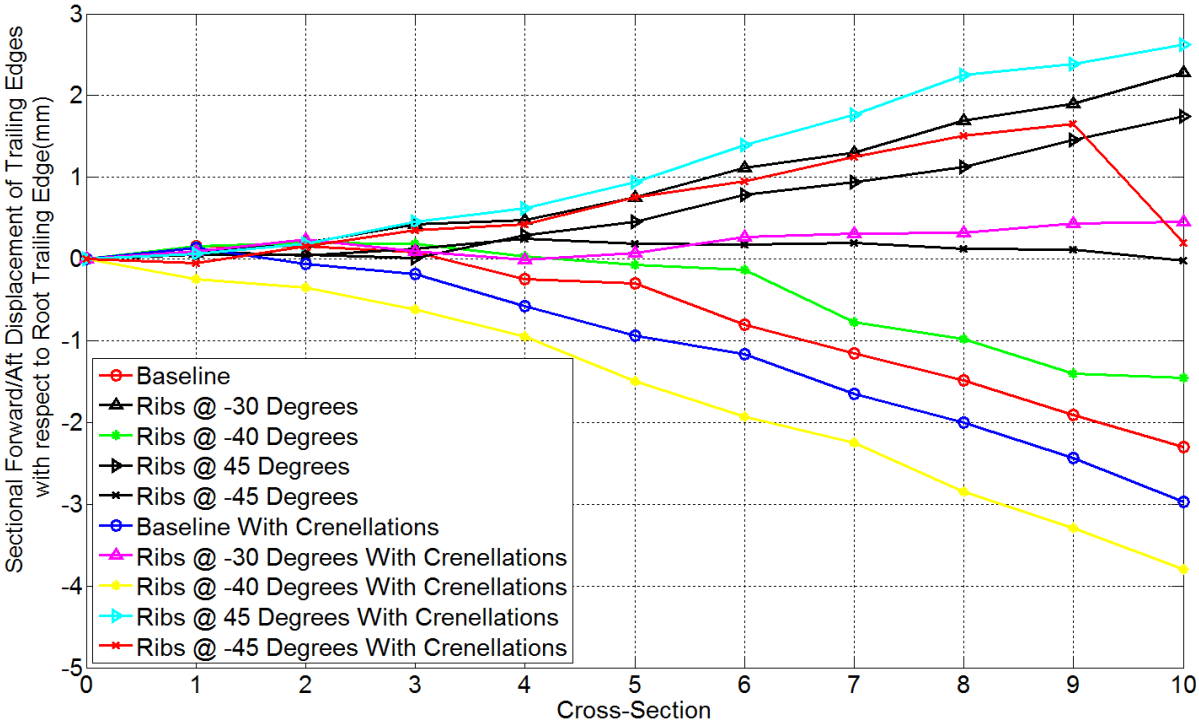

Figure 41. Sectional Forward/Aft Displacement of Section trailing edge with respect to the root trailing edge. Section 10 is at the wing tip.

DISTRIBUTION A. Approved for public release: distribution unlimited.

Table 9. Average and standard deviation sectional chord length for the wings of order 6.

	Average Sectional Chord Length (mm)	Standard Deviation Sectional Chord Length (mm)	Difference with CAD chord length (%)
Baseline	101.3	0.2	-0.7
Rib @ -30 Degrees	101.3	0.4	-0.6
Rib @ -40 Degrees	101.4	0.2	-0.6
Rib @ 45 Degrees	101.3	0.2	-0.7
Rib @ -45 Degrees	101.6	0.1	-0.4
Baseline With Crenellations	101.6	0.1	-0.4
Rib @ -30 Degrees With Crenellations	101.3	0.2	-0.7
Rib @ -40 Degrees With Crenellations	101.5	0.1	-0.4
Rib @ 45 Degrees With Crenellations	101.6	0.1	-0.4
Rib @ -45 Degrees With Crenellations	101.2	0.7	-0.8

7.1.1.1 Internal Measurements

In order to determine the tolerance of the internal dimensions microtomography analysis of several wings have been ordered. Table 10 shows the wings sent for microtomography analysis. The results are still being processed at this time.

Table 10. Wings sent for microtomography analysis.

Order Number	Wing Design	Orientation of Wing in Printer
1	Baseline	a
4	Baseline	c
5	Baseline	b
6	Baseline	b
1	Rib @ 45 Degrees With Crenellations	a
5	Ribs @ -45 Degrees With Crenellations	b
5	Ribs @ 45 Degrees With Crenellations	b
6	Rib @ -45 Degrees With Crenellations	b
6	Rib @ -45 Degrees With Crenellations	b

7.1.1.2 Repeatability Assessment through Mass Variation

For a given rib/crenellation orientation value the mass of the wing is independent of the rib/crenellation orientation sign. Thus in the present study, nine wing designs were printed at least twice. Since the CAD files used for those designs have not been altered between orders the repeatability of the printing process can be assessed by considering the mass of the wings prior to painting. A variation in mass could be the results of change in dimension tolerances or change in material density. The wing mass prior to painting was taken after the cleaning process. This is considered more accurate than the mass of the wings delivered by the manufacturer as they arrived with varying amount of trapped powder in the rib bays.

Figure 42 and Figure 43 show the mass variation of the different wing rib/crenellation orientation designs with the order number and print direction. Bearing in mind that some variation in mass can exist due to variation in the cleaning process it is interesting to notice that the direction at which the part is placed in the printer does not seem to have large impact on the wing mass. However large variations in

wing mass were recorded between different orders made with the same print direction. For example, when considering wings with ribs oriented at ±45º with and without crenellations, the wings printed for order 2 were 32.6% and 19.5% heavier than the ones printed for order 6, respectively.

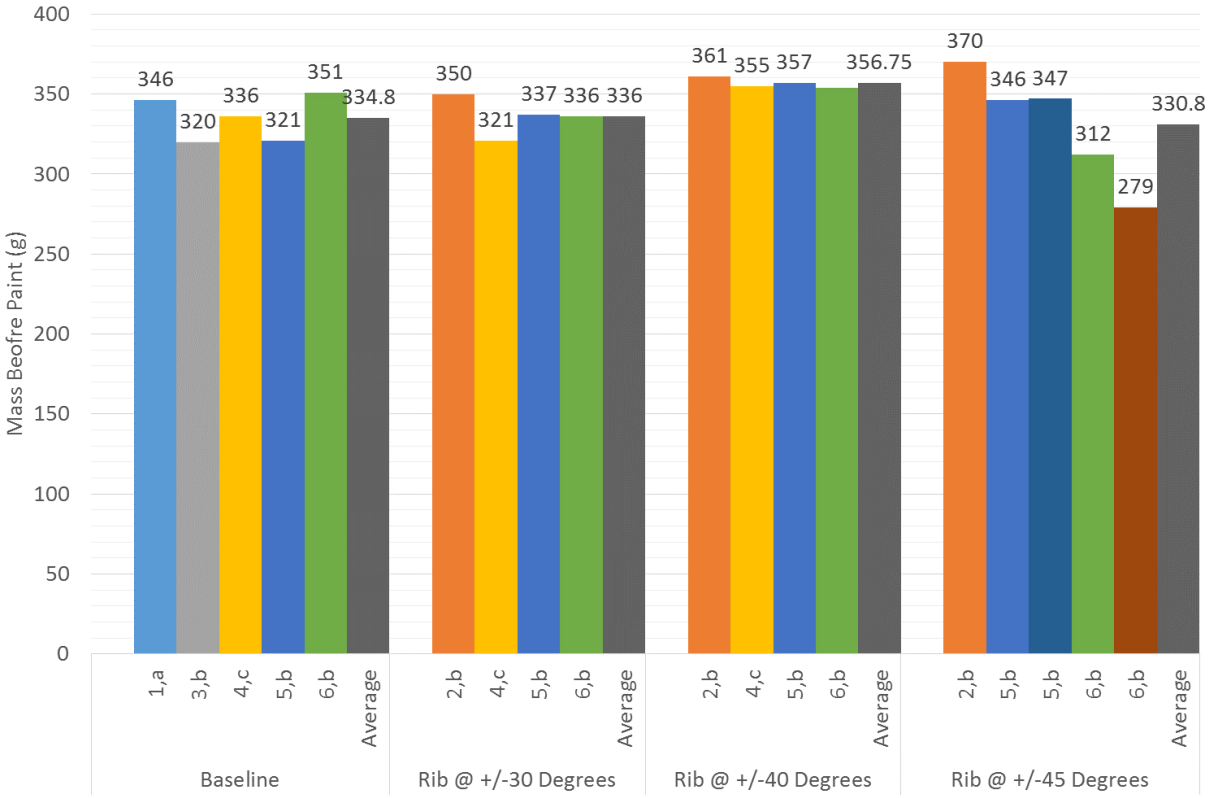

Figure 42. Mass of wings with ribs before painting and averages for the different designs, order number (1 to 6) and print direction (a, b or c).

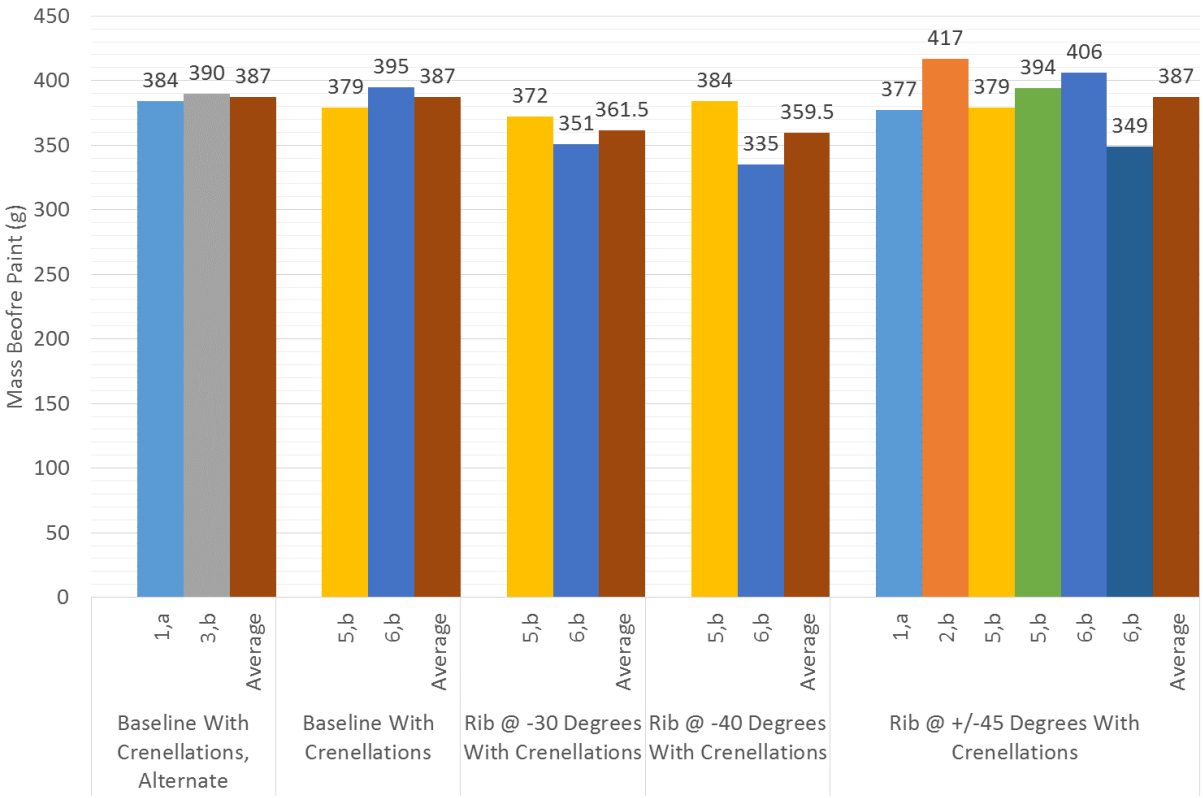

Figure 43. Mass of wings with ribs and crenellations before painting and averages for the different designs, order number (1 to 6) and print direction (a, b or c).

7 Experimental Results

In following sections only results from orders 2 and 3 are considered. Processing of data for the other orders is still on-going. These findings will be presented at a later date.

7.1 Static Experiment

Figure 44 and Figure 45 show the average displacement and twist at 15mm from the tip for the NACA profiled wing box (NWB) with no crenellations and with crenellation widths of 11.11mm noting that both FE and experimental results are presented. The FE analysis was performed assuming an elastic material with the three different tensile moduli (1,500MPa, 1,650MPa and 1,800MPa) to illustrate the effect of tensile modulus variation on the tip displacement and twist. The experimental results presented for each wing are the average of at least three experiment runs and the standard deviation for the experimental data is shown as error bars.

First, the FE results show that the impact of changing the rib orientation is highly similar for a rectangular and NACA profiled wing box. A noticeable difference is the lack of symmetry around the 0^{o} rib orientation for the NACA profiled wing box in the average tip displacement and tip twist curves. This result is due to the lack of geometric symmetry about the mid-chord depth plane of the NACA profiled wing box. This implies that a tip load at the mid-chord point has both bending and torsion components, as manifested by the existence of a tip twist in the 0^{o} rib orientation case.

The addition of the crenellation has a similar impact in both the rectangular wing box and the NACA profiled wing box: a reduction in the average tip displacement values and a reduction in the ordinate distance between the two stationary points of the cubic tip twist curve. Once again, the removal of the symmetry in the box depth removes the symmetry in the tip displacement and twist results.

It should be noticed that the difference in crenellation scheme for the wing with crenellations width of 11.11mm and 0^{o} rib/crenellation between the NACA profiled and the rectangular wing box models

explains the slight increase in tip displacement at 0° rib/crenellation orientation displayed by the NACA profiled model.

When considering the variation in rib orientation the trend predicted by FE results was also shown in the experimental results: reduction of the displacement and nose down twist as the rib orientation increases. For example, a variation of the rib orientation form 30° to 45° predicted a reduction in average tip displacement of 2.2% and 1.1% and a reduction in tip twist of 36.7% and 39.9% for the experiment and the FE results with a tensile modulus of 1,650MPa respectively.

The addition of crenellation at a given rib/crenellation orientation reduced the displacement and reduced the nose down twist in the experimental results as predicted by FE results. The impact of such reductions varies, however, between the FE and the experimental results. For example, for the rib/crenellation at an orientation of 45° the experiment and the FE results (E=1,650MPa) predicted a reduction in average tip displacement of 9.2% and 6.1%, respectively and a reduction in tip twist of 85.5% and 64.1%, respectively due to the crenellation concept. Indeed in the experimental results, the wing with rib/crenellation at 45° orientation showed a nose-up twist.

Although the major trends observed in the FE results were shown in the experimental results it is apparent that a variation existed between the experimental and FE results. It is believed that some of these variations are due to the material property variability observed in Section 5 and the viscoelastic nature of the material used. To illustrate the effect of material variability, stress relaxation and load history in an experiment where the load is not deformation dependent a reduction in the tensile modulus should reduce the error between the FE and experimental results. As shown by Figure 44 and Figure 45, the agreement between the FE and experimental results improves when a tensile modulus of 1,500MPa is used in the FE analysis. The maximum error in tip displacement and twist for wings with ribs orientation of 30°, 40° and 45° is reduced from 9.0% and 10.7% to -1.9%and -4.4% respectively when reducing the tensile modulus from 1,650MPa to 1,500MPa. It is believed that the larger errors seen in Figure 44 and Figure 45 are the result of manufacturing variability and material property variability. For example, in the experiment the wing with rib/crenellation at 45° displayed a positive twist when loaded. FE results predicted that this wing would have a nose-down twist under load. Further work is investigating those effects.

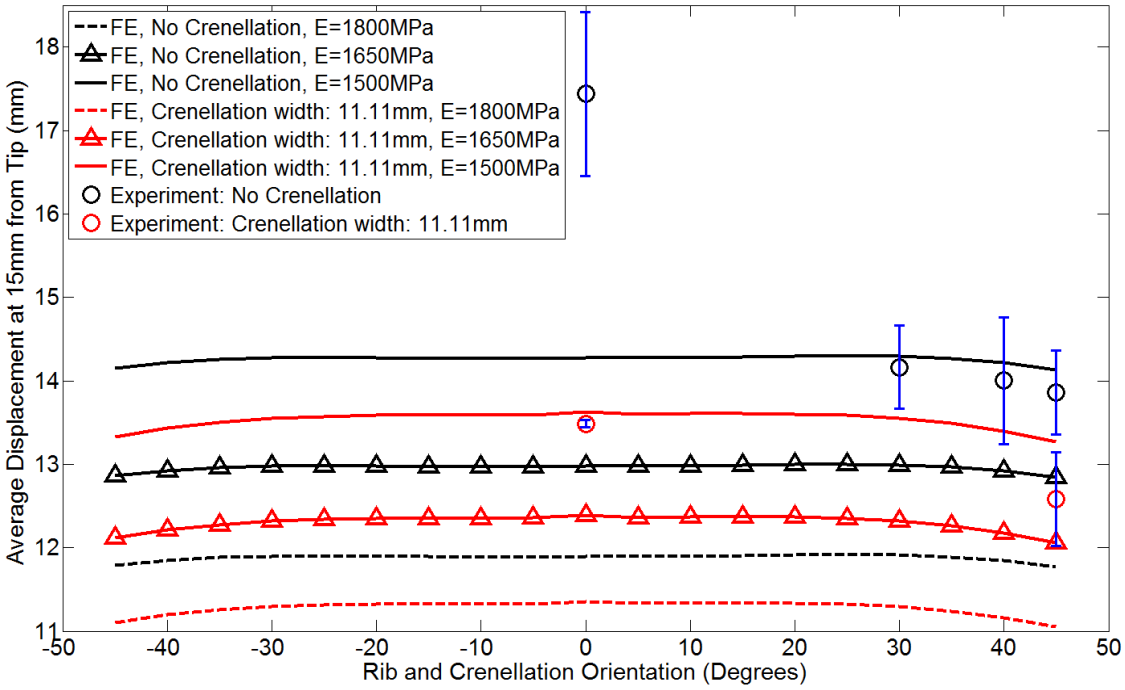

Figure 44. FE and experimental average displacement at 15mm from the tip for NACA profiled Wing Box (NWB) with no crenellation and crenellation (width: 11.11mm)

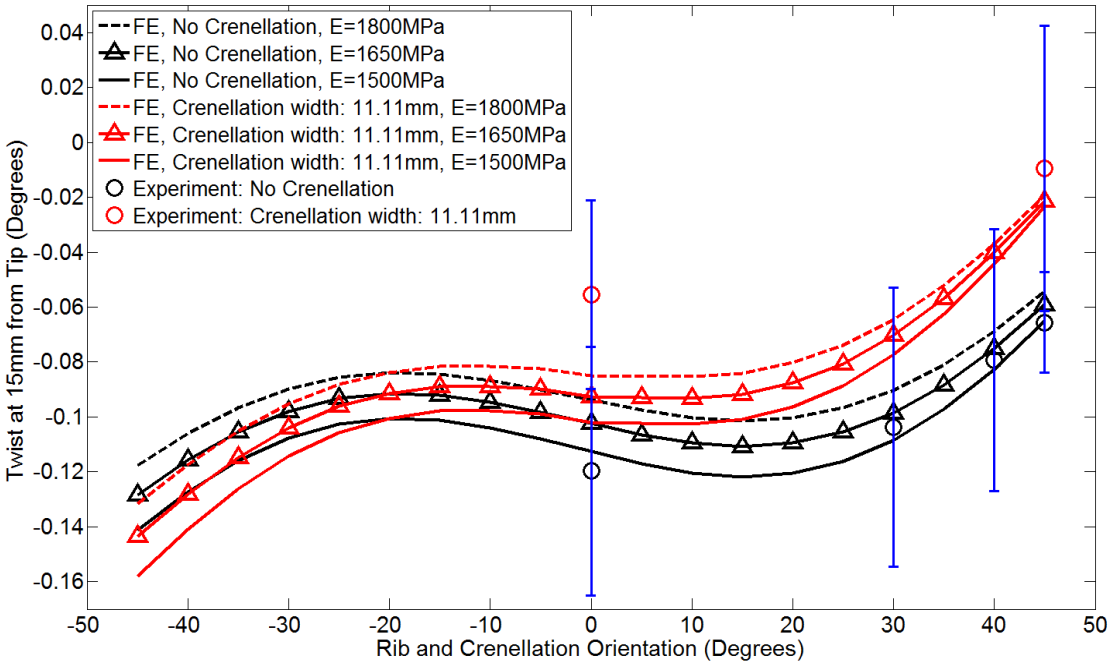

Figure 45. FE and experimental twist at 15mm from the tip for NACA profiled Wing Box (NWB) with no crenellation and crenellation (width: 11.11mm)

7.2 Aeroelastic Static Experiment Results

Figure 46 and Figure 47 show the average tip displacement and tip twist for NACA profiled wings with no crenellation and with crenellation of width 11.11mm with different rib/crenellation orientations when subject to aerodynamic loading. Both FE and experimental results are presented. The FE analysis was performed with three different tensile moduli assuming an elastic material. The experimental results for each wing presented are the average of three wind tunnel runs and the standard deviation for the experimental data is shown as error bars.

The FE results show that the use of a NACA profiled wing removed the symmetry in the tip displacement curve around the 0° rib/crenellation orientation, as previously shown. The addition of a load at the quarter chord magnifies this lack of symmetry. The addition of the crenellation reduces the tip displacement of the wings. The ordinate distance between the two stationary points of the cubic tip twist curve is found to reduce and at high rib/crenellation orientation the wing twist is increased by the presence of crenellation.

When considering the experimental results, the major trends of positively increasing the rib/crenellation orientations are respected: a reduction in tip displacement and an increase in positive tip twist. For example the addition of crenellation for wings with ribs at an orientation of 45° reduced the average tip displacement by 10.7% and 5.6% for experimental and FE results respectively and increased the positive tip twist by 41.9% and 14.8%. These variations between FE and experimental results can be explained by the material property variability shown in Section 5.

The tip twist values predicted by FE and the experimental values show a good level of accordance with a maximum difference of -15.1% (E=1,650MPa). However the difference between tip displacement values predicted by the FE results and the experiment results are much higher (91.6% in the case of the wing with rib at 0° assuming E=1,650MPa). This variation is larger than the difference observed between FE and experimental results in the static tip load case. This behaviour can be explained due to several factors. First, as shown in Section 5 the material used in the experiment had a viscoelastic behaviour but it was modelled as being elastic in the FE analysis. The viscoelastic behaviour of the wing was appropriately captured in the static experiment by reducing the tensile modulus but this approach is failing in the wind tunnel experiment as the load is deformation dependent. In the wind tunnel experiment the load is dependent of the wing twist deformation hence any additional twist deformation due to stress relaxation and load history leads to higher loads and so higher tip

deflection and twist. Additionally, the wind tunnel experiment introduces larger sources of errors through, for example, the angle of attack setting, the impact of any pre-twist created by warping of the wing during the manufacturing process, the control of the temperature in the wind tunnel and the aerofoil's surface finish in addition to the manufacturing and material property variability.

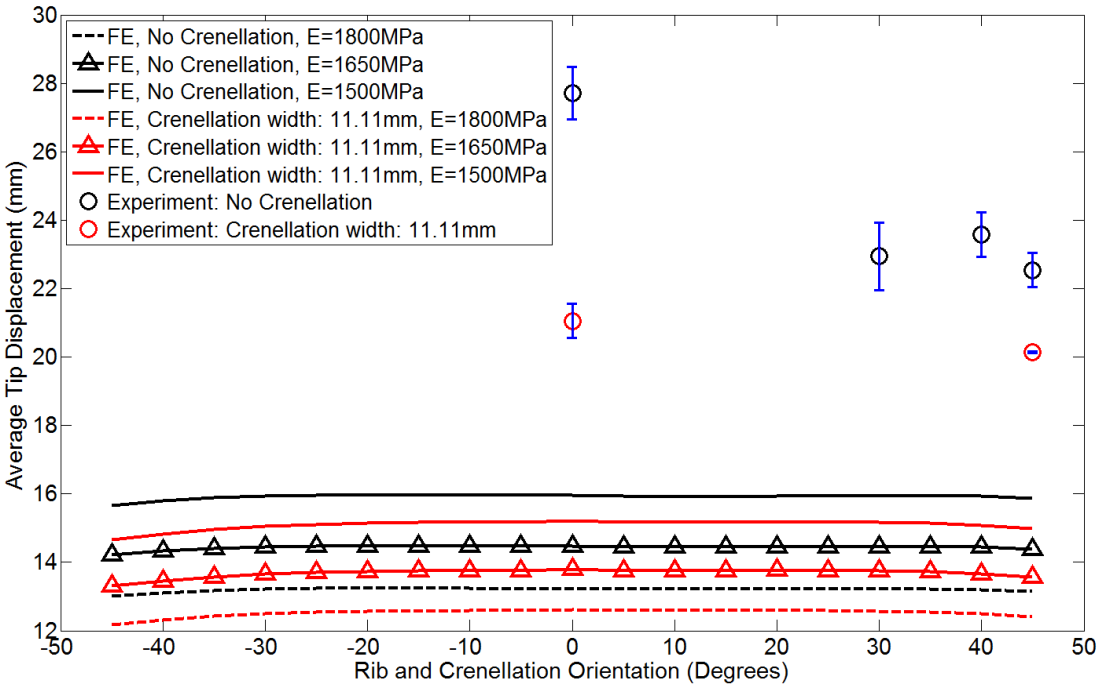

Figure 46. FE and experimental average tip displacement for NACA profiled Wing Box (NWB) with no crenellation and crenellation (width: 11.11mm) at an angle of attack of 5° and airspeed of 35m/s. The experimental results are the average of three wind tunnel runs per wing

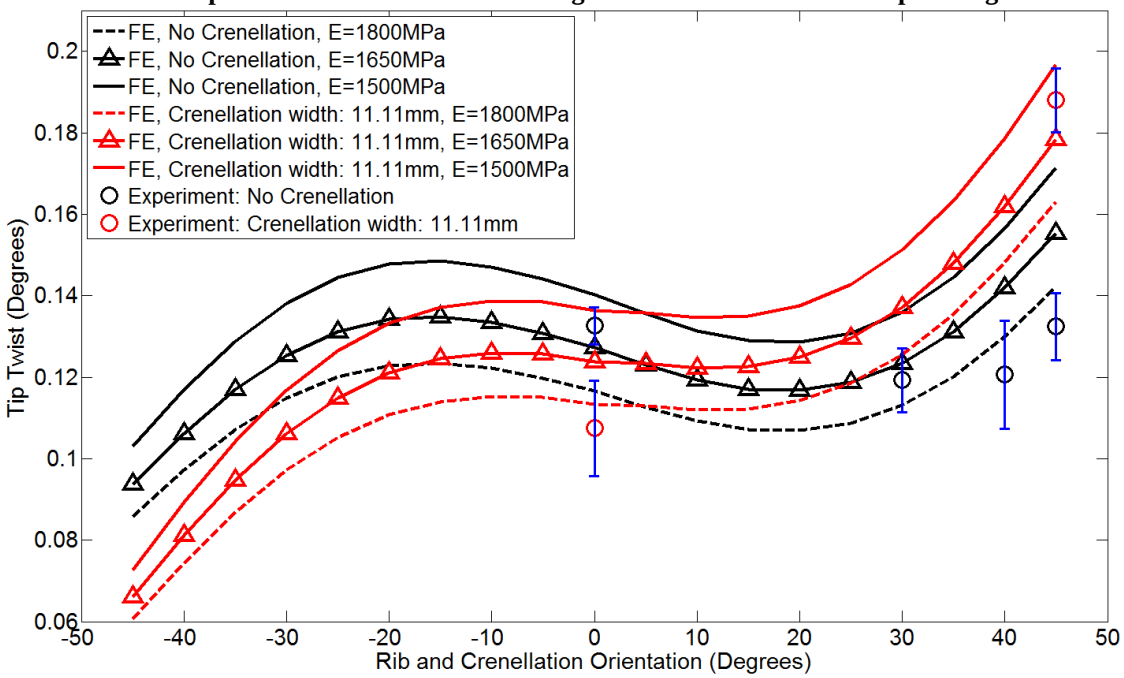

Figure 47. FE and experimental tip twist for NACA profiled Wing Box (NWB) with no crenellation and crenellation (width: 11.11mm) at an angle of attack of 5° and airspeed of 35m/s. The experimental results are the average of three wind tunnel runs per wing

7.3 Modal Experiment Results

Table 11 presents natural frequency data, damping and mode shapes for the first six modes found through modelling and experiment. It should be noted that both the FE and experiment agree on the

succession of mode shape with the only exception a forward/aft mode (for./aft) which the experiment could not determine due to the position of the accelerometer.

To compare the agreement between the FE and modelling results Table 12 shows the percentage difference in natural frequencies between the two types of results. The comparison is acceptable with a maximum of 14.5% difference for mode 1 and 2 and a maximum difference of 20.9% for mode 3, 4, 5 and 6.

Finally, Table 13 and Table 14 presents the difference in natural frequency between a wing with no crenellations, ribs at 0^o orientations and with the other wings considered. Both experimental and FE results are used. Clearly both set of results proved that by adding crenellations and changing the orientation of the rib/crenellation one can change the natural frequencies of the wing. It is interesting to note that although the addition of crenellation adds mass to the wing as shown in **Error! Reference source not found.** the change in rib/crenellation orientation has a larger impact on the natural frequencies.

Table 11 Experiment and modelling natural frequency, damping and shape results of the first five mode shape for the three wings manufactured.

	Ribs @ 0^o (R0), No Crenellation					Ribs/ Crenellation @ 0^o (R/C0), With Crenellation				
	Experiment			FE		Experiment			FE	
Mode	Freq. (Hz)	Damping %	Shape	Freq. (Hz)	Shape	Freq. (Hz)	Damping %	Shape	Freq. (Hz)	Shape
1	10.63	1.93	Bending	10.74	Bending	10.86	1.27	Bending	10.14	Bending
2	67.51	0.85	Bending	64.63	Bending	68.15	0.85	Bending	61.22	Bending
			For. /Aft	69.52	For. /Aft			For. /Aft	65.16	For. /Aft
3	107.05	0.94	Torsion	96.06	Torsion	114.06	0.86	Torsion	96.76	Torsion
4	186.06	1.23	Bending	171.62	Bending	187.65	0.69	Bending	163.16	Bending
5	321.03	1.05	Torsion	287.66	Torsion	340.37	0.64	Torsion	290.07	Torsion
6	355.28	0.95	Bending	312.47	Bending	354.23	0.88	Bending	298.84	Bending
	Ribs @ 30^o (R30), No Crenellation					Ribs @ 40^o (R40), No Crenellation				
	Experiment			FE		Experiment			FE	
Mode	Freq. (Hz)	Damping %	Shape	Freq. (Hz)	Shape	Freq. (Hz)	Damping %	Shape	Freq. (Hz)	Shape
1	11.60	0.95	Bending	10.52	Bending	11.54	0.89	Bending	10.48	Bending
2	70.94	1.01	Bending	63.57	Bending	71.19	0.81	Bending	63.44	Bending
			For. /Aft	68.05	For. /Aft			For. /Aft	67.79	For. /Aft
3	114.90	1.06	Torsion	96.69	Torsion	116.33	1.16	Torsion	96.96	Torsion
4	194.20	0.75	Bending	169.70	Bending	194.89	0.77	Bending	169.66	Bending
5	337.02	0.90	Torsion	289.14	Torsion	342.04	0.93	Torsion	289.85	Torsion
6	365.17	0.78	Bending	310.88	Bending	366.68	0.79	Bending	311.44	Bending
	Ribs @ 45^o (R45), No Crenellation					Ribs/ Crenellation @ 45^o (R/C45), With Crenellation				
	Experiment			FE		Experiment			FE	
Mode	Freq. (Hz)	Damping %	Shape	Freq. (Hz)	Shape	Freq. (Hz)	Damping %	Shape	Freq. (Hz)	Shape
1	11.29	1.18	Bending	10.46	Bending	11.16	0.81	Bending	10.00	Bending
2	70.88	0.78	Bending	63.40	Bending	69.51	0.69	Bending	60.70	Bending
			For./Aft	67.73	For. /Aft			For. /Aft	63.78	Forward/ Aft
3	114.37	1.05	Torsion	96.99	Torsion	118.76	1.05	Torsion	98.31	Torsion
4	194.72	0.74	Bending	169.73	Bending	191.17	0.68	Bending	162.80	Bending
5	343.52	0.82	Torsion	289.87	Torsion	350.80	0.92	Torsion	292.98	Torsion
6	364.88	0.92	Bending	311.97	Bending	363.20	0.94	Bending	300.40	Bending

DISTRIBUTION A. Approved for public release: distribution unlimited.

Table 12 Percentage difference in natural frequencies for the first six mode shape between modelling and FE results.

	% Difference Between Experiment and FE					
Mode	R0	R/C0	R30	R40	R45	R/C45
1	-1.0	7.1	10.3	10.1	7.9	11.6
2	4.5	11.3	11.6	12.2	11.8	14.5
	100.0	100.0	100.0	100.0	100.0	100.0
3	11.4	17.9	18.8	20.0	17.9	20.8
4	8.4	15.0	14.4	14.9	14.7	17.4
5	11.6	17.3	16.6	18.0	18.5	19.3
6	13.7	18.5	17.5	17.7	17.0	20.9

Table 13 Experimental natural frequencies percentage difference between a wing with no crenellations and wings with varying rib/crenellation orientation

	% Difference with respect to R0, No Crenellation - Experiment				
Mode	R/C0	R30	R40	R45	R/C45
1	2.2	9.1	8.6	6.2	5.0
2	0.9	5.1	5.4	5.0	3.0
3	6.5	7.3	8.7	6.8	10.9
4	0.9	4.4	4.7	4.7	2.7
5	6.0	5.0	6.5	7.0	9.3
6	-0.3	2.8	3.2	2.7	2.2

Table 14 Finite Element natural frequencies percentage difference between a wing with no crenellations and wings with varying rib/crenellation orientation

	% Difference with respect to R0, No Crenellation - FE				
Mode	R/C0	R30	R40	R45	R/C45
1	-5.5	-2.0	-2.4	-2.6	-6.9
2	-5.3	-1.6	-1.8	-1.9	-6.1
	-6.3	-2.1	-2.5	-2.6	-8.2
3	0.7	0.7	0.9	1.0	2.3
4	-4.9	-1.1	-1.1	-1.1	-5.1
5	0.8	0.5	0.8	0.8	2.2
6	-4.4	-0.5	-0.3	-0.2	-3.9

8 Conclusions and Future Work

The project presented in this report aimed to model and experimentally validate the impact on the wing deformation of the following three concepts: the orientation between the ribs and spars, the crenelated skin and the curvilinear structure.

FE modelling of the different concepts has been performed. In the present report the rib/crenellation orientation, the crenellation width and thickness were used to control the tip displacement, tip twist and the wing's natural frequencies. It was shown that the rib orientation changed the wing bend-twist coupling and this variation can be increased by the crenellated skin concept. This leads to a maximum increase in flutter/divergence speed by 14.2% using the rib/crenellations orientations. Coupling the ribs and the crennellations together gave a much greater effect than each applied individually.

To validate FE analysis trends this project aimed to use 3D printed wings in wind-on/off structural tests and modal test. After extensive material testing, a SLS polyamide material was chosen. Several

orders of different wing structural designs were placed to quantify the impact of the wing structural designs on the wing performance and to assess the potential of commercially available 3D printing in aeroelastic experiments.

At this stage of the project, only a subset of the orders have been fully tested. These results validated the increase in stiffness linked with the crenellated skin and the increase in rib/crenellation orientation since the FE results. However, some significant differences were recorded between the FE and experimental results in the aeroelastic experiment. This effect is still being investigated but is believed to be strongly affected by the consistency and quality of the manufacturing technique (3D printing) and materials used. Initial material testing has quantified some of these effects, the direction in which the test coupons are printed has a large influence upon the material properties, but there are still significant variations as well.

9 Acknowledgments

The authors are grateful for the funding supplied by the AFOSR via the EOARD which enabled this work to be undertaken. In particular, the help and guidance of Matt Snyder is acknowledged.

10 Publications Resulting from this Work

G. François, J. E. Cooper & P. M. Weaver, 'Aeroelastic Tailoring using Crenellated Skins – Modelling and Experiment', *Accepted for publication in Advances in Aircraft and Spacecraft Science (2016)*.

G. François, J. E. Cooper & P. M. Weaver, 'Impact of the Wing Sweep Angle and Rib Orientation on Wing Sructural Response for Un-Tapered Wings', *57th AIAA/ASCE/AHS/ASC Structures, Structural Dynamics, and Materials Conference*, 4-8 January 2016, San Diego, California, USA.

G. Francois, J. E. Cooper & P. M. Weaver, 'Aeroelastic Tailoring using Crenellated Skins – Modelling and Experiment', *International Forum on Aeroelasticity and Structural Dynamics*, June 28-July 2, 2015, Saint Petersburg, Russia.

G. Francois, J. E. Cooper & P. M. Weaver, 'Aeroelastic Tailoring using Rib/Spar Orientations: Experimental Investigation', *56th AIAA/ASCE/AHS/ASC Structures, Structural Dynamics, and Materials Conference*, 5-9 January 2015, Kissimmee, Florida, USA.

G. François, J. E. Cooper & P. M. Weaver, 'Aeroelastic Tailoring of Composite Wings using Internal Structural Members Shape and Stacking Sequence', 2014, *Proceeding of the Royal Aeronautical Society 4th Aircraft Structural Design Conference*, 7-9 October 2014, Belfast ,UK.

G. François & J. E. Cooper, 'Novel Structural Wing Designs for Forward Swept Wings', 2014, *Proceeding of the 2014 Royal Aeronautical Society Biennial Applied Aerodynamics Research Conference*, 22-24 July 2014, Bristol ,UK.

11 References

[1] Airbus, "Future Journeys 2013-2032," 2013. [Online]. Available: http://www.airbus.com/company/market/forecast/?eID=dam_frontend_push&docID=33752. [Accessed: 08-May-2015].

[2] J. R. Wright and J. E. Cooper, *Introduction to Aircraft Aeroelasticity and Loads*. Wiley, 2007.

[3] M. H. Shirk, T. J. Hertz, and T. A. Weisshaar, "Aeroelastic tailoring-theory, practice, and promise," *Journal of Aircraft*, vol. 23, no. January 1986, pp. 6–18, 1986.

DISTRIBUTION A. Approved for public release: distribution unlimited.

[4] F. E. Eastep, V. A. Tischler, V. B. Venkayya, and N. S. Khot, "Aeroelastic tailoring of composite structures," *Journal of aircraft*, vol. 36, no. 6, pp. 1041–1047, 1999.
[5] T. Kim and I. H. Hwang, "Optimal design of composite wing subjected to gust loads," *Computers & Structures*, vol. 83, no. 19–20, pp. 1546–1554, Jul. 2005.
[6] S. Guo, "Aeroelastic optimization of an aerobatic aircraft wing structure," *Aerospace Science and Technology*, vol. 11, no. 5, pp. 396–404, Jun. 2007.
[7] S. Guo, D. Li, and Y. Liu, "Multi-objective optimization of a composite wing subject to strength and aeroelastic constraints," *Proceedings of the Institution of Mechanical Engineers, Part G: Journal of Aerospace Engineering*, vol. 226, no. 9, pp. 1095–1106, Oct. 2011.
[8] A. Manan, G. A. Vio, M. Y. Harmin, and J. E. Cooper, "Optimization of aeroelastic composite structures using evolutionary algorithms," *Engineering Optimization*, vol. 42, no. 2, pp. 171–184, Feb. 2010.
[9] O. Stodieck, J. E. Cooper, P. M. Weaver, and P. Kealy, "Optimisation of Tow - Steered Composite Wing Laminates for Aeroelastic Tailoring," in *53th AIAA/ASMe/ASCE/AHS/SC Structures, Structural Dynamics, and Material Conference, National Harbor, Maryland, USA*, 2014, no. January.
[10] C. V. Jutte, B. K. Stanford, C. D. Wieseman, and J. B. Moore, "Aeroelastic Tailoring of the NASA Common Research Model via Novel Material and Structural Configurations," in *53th AIAA/ASMe/ASCE/AHS/SC Structures, Structural Dynamics, and Material Conference, National Harbor, Maryland, USA*, 2014, no. January, pp. 1–20.
[11] M. P. Bendsøe and O. Sigmund, *Topology Optimization Theory, Methods and Applications*. Springer, 2003.
[12] K. Maute and M. Allen, "Conceptual design of aeroelastic structures by topology optimization," *Structural and Multidisciplinary Optimization*, vol. 27, no. 1–2, pp. 27–42, May 2004.
[13] C. J. Brampton, H. A. Kim, and J. L. Cunningham, "Level Set Topology Optimisation of Aircraft Wing Considering Aerostructural Interaction," in *12th AIAA Aviation Technology, Integration, and operations (ATIO) Conference and 14th AIAA/ISSM 17-19 September 2012, Indianapolis, Indiana, United States of America*, 2012, no. September, pp. 1–10.
[14] P. D. Dunning, B. K. Stanford, and H. A. Kim, "Aerostructural Level Set Topology Optimization for a Common Research Model Wing," in *10th AIAA Multidisciplinary Design Optimization Conference, 13-17 January 2014, National Harbor, Maryland, USA*, 2014, no. January, pp. 1–21.
[15] P. D. Dunning, B. K. Stanford, and H. A. Kim, "Level - Set Topology Optimization with Aeroelastic Constraints," in *56th AIAA/ASMe/ASCE/AHS/SC Structures, Structural Dynamics, and Material Conference, Kissimmee, Florida, USA*, 2015, no. January, pp. 1–19.
[16] R. M. Kolonay and M. H. Kobayashi, "Topology, Shape, and Sizing Optimization of Aircraft Lifting Surfaces Using a Cellular Division Method," in *13th AIAA/ISSMO Multidisciplinary Analysis Optimization Conference, Forth Worth, Texas, United States of America*, 2010, no. September.
[17] M. Y. Harmin, A. T. Ahmed, J. E. Cooper, and F. Bron, "Aeroelastic Tailoring of Metallic Wing Structures," in *52nd AIAA/ASME/ASCE/AHS/ASC Structures, Structural Dynamics and Materials Conference, 4-7 April 2011, Denver, Colorado, United States Of America*, 2011, no. April, pp. 1–19.
[18] G. A. Vio and I. R. Fitzpatrick, "Design of Composite Structures for Improved Aeroelastic Performance," *28th ICAS, 23-28 September 2012, Brisbane, Australia*, pp. 1–9, 2012.
[19] G. A. Vio, G. Georgiou, and J. E. Cooper, "Design of Composite Structures to Improve the Aeroelastic Performance," in *53rd AIAA/ASME/ASCE/AHS/ASC Structures, Structural Dynamics and Materials Conference, 23-26 April 2012, Honolulu, Hawai, United States Of America*, 2012, no. April, pp. 1–13.
[20] D. Locatelli, S. B. Mulani, and R. K. Kapania, "Wing-Box Weight Optimization Using Curvilinear Spars and Ribs (SpaRibs)," *Journal of Aircraft*, vol. 48, no. 5, pp. 1671–1684, Sep. 2011.
[21] Q. Liu, S. Mulani, and R. K. Kapania, "Global / Local Multidisciplinary Design Optimization of Subsonic Wing," in *53th AIAA/ASMe/ASCE/AHS/SC Structures, Structural Dynamics, and*

Material Conference, National Harbor, Maryland, USA, 2014, no. January, pp. 1–17.
[22] Q. Liu, M. Jrad, S. B. Mulani, and R. K. Kapania, "Integrated Global Wing and Local Panel Optimization of," in *56th AIAA/ASMe/ASCE/AHS/SC Structures, Structural Dynamics, and Material Conference, Kissimmee, Florida, USA*, 2015, no. January, pp. 1–19.
[23] M. C. Y. Niu, *Airframe Structural Design*, 2nd Editio. Hong Kong Conmilit Press Ltd, 1999.
[24] J. A. Samareh, "A survey of shape parameterization techniques," in *CEAS/AIAA/ICASE/NASA Langley International Forum on Aeroleasticity and Structural Dynamics, Williamsburg, Virginia, United States of America*, 1999, no. June, pp. 333–343.
[25] J. Kennedy and R. Eberhart, "Particle swarm optimization," in *IEEE International Conference on Neural Networks, Perth, WA*, 1995, vol. 4, pp. 1942–1948.
[26] R. Tatham, "Shear Centre, Flexural Centre and Flexural Axis: An Attempt to Clear up Current Confusion and Provide Definitions Differentiating Between the Three Terms," *Aircraft Engineering and Aerospace Technology*, vol. 23, no. 7, pp. 209–210, 1951.
[27] O. Stodieck, J. E. Cooper, and P. M. Weaver, "On the Interpretation of Bending-Torsion Coupling for Swept, Non-Homogenous Wings," in *56th AIAA/ASMe/ASCE/AHS/SC Structures, Structural Dynamics, and Material Conference, Kissimmee, Florida, USA*, 2015, pp. 1–28.
[28] W. P. Rodden and E. H. Johnson, *MSC/NASTRAN Aeroelastic Analysis User's Guide v68*. The MacNeal-Schwendler Corporation, 1994.
[29] H. H. Khodaparast, G. Georgiou, J. E. Cooper, U. Kingdom, L. Travaglini, G. A. Vio, P. Denner, and F. Engineer, "Rapid Prediction of Worst Case Gust Loads," in *52nd AIAA/ASME/ASCE/AHS/ASC Structures, Structural Dynamics and Materials Conference, 4-7 April 2011, Denver, Colorado, United States Of America*, 2011, no. April, pp. 1–22.
[30] E. H. Johnson, "MSC Developments in Aeroelasticity," in *1997 MSC Aerospace Users' Conference*, 1997, pp. 1–9.
[31] Imetrum, "Tensile Testing," 2016. [Online]. Available: http://www.imetrum.com/. [Accessed: 01-Feb-2016].
[32] FARO, "FARO ScanArm," 2016. [Online]. Available: http://www.faro.com/products/metrology/faro-scanarm/features#main. [Accessed: 23-May-2016].

DISTRIBUTION A. Approved for public release: distribution unlimited.